AFRL-AFOSR-JP-TR-2019-0051

Satellite Wind Tunnel Studies for LEO Objects in the Ionosphere

Philippe Lorrain
University of New South Wales-NEW NCAGE Code
HIGH STREET
KENSINGTON, NSW, 2052
AU

08/14/2019
Final Report

Air Force Research Laboratory
Air Force Office of Scientific Research
Asian Office of Aerospace Research and Development
Unit 45002, APO AP 96338-5002

REPORT DOCUMENTATION PAGE

Form Approved
OMB No. 0704-0188

1. REPORT DATE *(DD-MM-YYYY)*	2. REPORT TYPE	3. DATES COVERED *(From - To)*
14-08-2019	Final	08 Sep 2017 to 07 Sep 2018

4. TITLE AND SUBTITLE
Satellite Wind Tunnel Studies for LEO Objects in the Ionosphere

5a. CONTRACT NUMBER

5b. GRANT NUMBER
FA2386-17-1-4105

5c. PROGRAM ELEMENT NUMBER
61102F

6. AUTHOR(S)
Philippe Lorrain

5d. PROJECT NUMBER

5e. TASK NUMBER

5f. WORK UNIT NUMBER

7. PERFORMING ORGANIZATION NAME(S) AND ADDRESS(ES)
University of New South Wales-NEW NCAGE Code
HIGH STREET
KENSINGTON, NSW, 2052 AU

8. PERFORMING ORGANIZATION REPORT NUMBER

9. SPONSORING/MONITORING AGENCY NAME(S) AND ADDRESS(ES)
AOARD
UNIT 45002
APO AP 96338-5002

10. SPONSOR/MONITOR'S ACRONYM(S)
AFRL/AFOSR IOA

11. SPONSOR/MONITOR'S REPORT NUMBER(S)
AFRL-AFOSR-JP-TR-2019-0051

12. DISTRIBUTION/AVAILABILITY STATEMENT
A DISTRIBUTION UNLIMITED: PB Public Release

13. SUPPLEMENTARY NOTES

14. ABSTRACT

The evolving nature of the challenges facing LEO activities requires advances in space traffic management capabilities that are contingent on an understanding of all the forces affecting a bodys motion. The aerodynamic interaction of LEO objects with the ionosphere (ionospheric aerodynamics) is currently not considered. This work presented a review of the early charged drag experiment performed by Knechtel and Pitts [1] and comparisons with predictions made using the PIC-DSMC code, pdFOAM. While uncertainties in the experimental description made an accurate reconstruction of the results in [1] difficult, the following observations were made: pdFOAM was successfully able to reproduce trends observed experimentally in [1]; scaling of plasma-body interactions must be able to account for artificial body potentials; the design of experiments should carefully consider the coupling of phenomena if using body potential as a test parameter; and the increase in charged drag forces on the small test model studied by Knechtel and Pitts [1] may have been primarily caused by an increase in relative sheath thickness (and direct drag forces) instead of indirect effects as previously hypothesized.

15. SUBJECT TERMS
wind tunnel, satellite drag, ionosphere

16. SECURITY CLASSIFICATION OF:			17. LIMITATION OF ABSTRACT	18. NUMBER OF PAGES	19a. NAME OF RESPONSIBLE PERSON
a. REPORT	b. ABSTRACT	c. THIS PAGE			WINDER, SHEENA
Unclassified	Unclassified	Unclassified	SAR		19b. TELEPHONE NUMBER *(Include area code)* +81-42-511-2008

Standard Form 298 (Rev. 8/98)
Prescribed by ANSI Std. Z39.18

Final Report for AOARD Grant FA2386-17-1-4105

Satellite wind tunnel studies for LEO objects in the ionosphere

March 29, 2019

Dr. Philippe Lorrain[1,a)], Dr. Christopher Capon[1], Dr. Melrose Brown[1], Prof. Russell Boyce[1], Dr. Cormac Corr[2], Prof. Andrew Ketsdever[3] and Dr. Carlos Maldonado[4]

[1]*University of New South Wales Canberra, Canberra, ACT 2610, Australia.*
[2]*Australian National University, Canberra, ACT 0200, Australia.*
[3]*Oregon State University Cascades, Bend, OR 97702, U.S.A.*
[4]*United States Air Force Academy, CO, U.S.A.*

[a)]Corresponding author: p.lorrain@unsw.edu.au, +61 (2) 6268 8522

Period of Performance: 09/08/2017 to 09/07/2018

Abstract

Addressing current risks and future opportunities associated with the utilization of space-based technologies requires advances in our ability to understand and accurately and rapidly predict the physics of the manner in which resident space objects (RSOs) interact with the space environment – both operational satellites and space debris. Effective space traffic management in an increasingly congested Low Earth Orbit (LEO) environment relies upon an thorough understanding of all the forces influencing a RSO's motion to enable precise orbit prediction and determination. Drag from the neutral atmosphere is widely known to contribute the greatest uncertainty to along-track position for LEO RSOs. However, recent numerical research conducted at UNSW Canberra revealed the possibility that an additional non-conservative force component arising from the interaction of a charged body with the rarefied plasma within the ionosphere (charged aerodynamics) could contribute an appreciable additional force.

The purpose of this research project was to develop a coupled experimental and numerical approach for fundamental studies of charged aerodynamics in the LEO context and, specifically, to demonstrate the ability to obtain experimental charged force measurements for representative LEO plasma/body interaction conditions in ground-based testing facility.

The objectives of the project were achieved through a collaboration with the University of Colorado Colorado Springs (UCCS) and the Australian National University Advanced Instrumentation and Technology Center (AITC) and leveraging the high-fidelity numerical modeling capability for simulating LEO plasma/body interactions being developed at UNSW Canberra. The established space simulation facility at UCCS was used to perform the experimental charged aerodynamics work for this project. The experimental efforts were complemented by numerical simulations using the UNSW Canberra in-house coupled particle-in-cell (PIC)/Direct Simulation Monte Carlo (DSMC) code pdFoam to gain further insight into the fundamental physical mechanisms underlying the observed trends. Charged force measurements were performed successfully for a 3.5 in square and 5 mm thick Aluminium plate mounted on a nano-Newton force balance and immersed in a ≈ 4.9 eV streaming Argon ion plasma flow representative of a LEO-like plasma/body interaction. The plasma flow was produced by a magnetic filter type plasma source and plasma flow properties were determined from Langmuir Probe (LP) and Retarding Potential Analyzer (RPA) measurements. Force measurements were collected for a range of plate surface potentials between 0 V and -500 V at -50 V increments. The nano-Newton force balance employed in this study was shown to be capable of resolving the changes in the net charged force on the test object with varying applied surface potential. The ion current collected by the charged test object during the tests was measured as a proxy for direct momentum exchange from streaming ions impacting on the test object surfaces.

The combination of force and current measurements, specifically the difference in the observed trends, has provided experimental evidence for the existence of a force counteracting the direct charged force (from ion impact) imparted on the charged test object. This effect results from an indirect, electrostatic interaction between the charged particle stream and the charged test object causing an increase in indirect forces with increasing negative surface potential. While hypothesized by other researchers and shown numerically in the past, this is the first experimental dataset directly indicating the competing action of direct and indirect charged forces for LEO-like plasma/body interactions.

Numerical reconstructions of the present experiments revealed that the observed effect is related to the electrostatic interaction between the streaming ions and the sheath surrounding the charged test object. The relative sheath thickness compared to the size of the test object was identified as a key parameter governing the observed behavior. Further numerical simulations showed that for the same test object surface potential charged forces become more appreciable as the test object becomes smaller owing to the larger relative sheath thickness causing a relative increase in direct drag.

These findings are significant in the context of the growing space debris population in LEO, which is made up in part of a large number of small objects, e.g. fragments from breakups or collisions, in that smaller objects are expected to be more susceptible to enhanced ionospheric aerodynamics effects. Therefore, perturbations from ionospheric aerodynamics effects should be accounted for to improve the accuracy of precise orbit determination models. Furthermore, the work presented in this report demonstrates the importance of careful consideration of

the relevant scaling laws when studying ionospheric aerodynamics in ground-based testing facilities. The research findings are summarized in the two publications included in Appendix A and B of this report.

In addition to the experimental work conducted in collaboration with UCCS, the first stage of commissioning a ground-based experimental ionospheric aerodynamics research capability by UNSW Canberra was completed within the scope of this project. A Low Earth Orbit Plasma Source (LEOPS), the same magnetic filter type plasma source employed for the experimental work at UCCS, was installed in the Space Simulation Facility (S2F) at the AITC. A successful plasma flow characterization campaign was conducted for a nominal 4.9 eV streaming Argon ion plasma flow providing spatially resolved plasma density, electron temperature and ion temperature measurements. Plasma densities were in the range 2.9×10^{14} m^{-3} to 4×10^{13} m^{-3} between 0.3 m and 0.8 m downstream of the plasma source. Electron and ion temperatures ranged from 0.35 eV to 0.38 eV, and 0.1 eV to 0.14 eV, respectively. The characterization tests have provided the foundation for ongoing experimental ionospheric aerodynamics research. The results are presented in detail in Appendix C of this report.

The work performed within the scope of this project has demonstrated that the established ground-based experimental research capability in conjunction with our numerical modeling capability represents a powerful research tool to address the gaps in our understanding of the physical processes underpinning plasma/body interactions in the ionosphere in LEO. The outcomes from this research will eventually feed into the development of advanced orbit propagation and collision-avoidance algorithms for Australian input to space traffic and debris management.

Contents

Appendix A

Early Experimental Ionosphere Drag Measurements Compared with Numerical Predictions Using pdFoam

(Peer-reviewed conference paper from the 31st Symposium on Rarefied Gas Dynamics in AIP conference proceedings.)

Early experimental ionosphere drag measurements compared with numerical predictions using pdFOAM

C.J. Capon[1,a)], P. Lorrain[1], M. Brown[1] and R. R. Boyce[1]

[1]*University of New South Wales Canberra, Canberra, ACT, Australia, 2612*

[a)]Corresponding author: c.capon@unsw.edu.au

Abstract. Space traffic management in a congested Low Earth Orbit (LEO) environment requires an understanding of all the forces influencing a body's motion to enable essential precise orbit prediction and determination capabilities. Among these forces, satellite aerodynamics represents a significant source of uncertainty. A neglected aspect of the satellite aerodynamics problem is the charged aerodynamic interaction of LEO objects with the ionosphere, i.e. ionospheric aerodynamics. To improve our understanding of ionospheric aerodynamics, this work numerically reproduces early experimental measurements by Knechtel and Pitts [1] of the ratio of charged to neutral drag ($F_{D,C}/F_{D,N}$) on spherical test models in a streaming Hg plasma using the Particle-in-Cell/Direct Simulation Monte Carl code, pdFOAM. Results demonstrate that pdFOAM is able to reproduce experimental trends in $F_{D,C}/F_{D,N}$ with body surface potential (ϕ_B) and model radii (r_B). Numerical observations indicate that, for the cases considered, direct drag forces (from ion/surface collisions) represented the primary source of the increase in $F_{D,C}/F_{D,N}$ with decreasing sphere radii. The relative increase in indirect drag forces (from non-colliding deflected ions) with decreasing radii was observed to become significant when the plasma scaling parameter α (energy ratio) was greater than 0.5. These trends appear to be caused by changes in relative sheath thickness as predicted by the plasma scaling parameter χ (shielding ratio). α and χ are both scaled by ϕ_B however, making it difficult to conclusively link underlying physical phenomena with observed $F_{D,C}/F_{D,N}$ trends with ϕ_B. A key recommendation for future experiments is to independently study the influence of these parameters on ionospheric aerodynamics.

INTRODUCTION

The sustainable development of the Low Earth Orbit (LEO) environment requires advances in space traffic management capabilities to address the challenges faced as LEO becomes increasingly congested. To achieve these capabilities, models must account for all the forces affecting the dynamics of these objects. LEO aerodynamics remains one of the most significant sources of uncertainty inhibiting these capabilities [2]. This uncertainty is commonly thought to arise from the convolution of uncertainties in the neutral drag coefficient ($C_{D,N}$) resulting from gas-surface interaction models [3] and uncertainties in atmospheric models predictions [4]. Not considered is the charged aerodynamics interaction between LEO objects and the ionosphere, i.e. ionospheric aerodynamics.

The reason for neglecting the contribution of ionospheric aerodynamic forces derives from arguments made by Brundin [5], referenced in the seminal work neutral drag work by Cook [6]. Not all early works agreed with the conclusions made in [5]. Disagreements revolved around the physical treatment of the system and assumptions therein [7, 8, 9, 10]. In an attempt to address these disagreements, Knechtel and Pitts [1] investigated the effect of body surface potential (ϕ_B) and body radii (r_B) on the drag forces on spherical test models in a streaming Mercury (Hg) plasma.

Knechtel and Pitts [1] compared their observations with available charged drag theories and concluded that the treatment proposed by Jastrow and Pearse [7] provided the best approximation of their observations. This result is notable as, while [5] and [7] considered physically similar systems, they came to opposing conclusions regarding the significance of ionospheric aerodynamics to the motion of LEO object. This disagreement largely stemmed from assumptions around ϕ_B - $\phi_B = O(-0.75V)$ [5], $\phi_B = O(-60V)$ [7]. While floating potentials $O(-0.75V)$ were later concluded to be (and are) the more reasonable assumption for a majority of LEO conditions [11, 12], recent advances have highlighted regions where LEO objects may naturally charge to high voltages [13, 14]. Active power systems on space platforms can also cause high artificial surface potentials [13, 14]. For example, McHarg *et al.* [15] measured spacecraft floating potentials between −25 and −35 V on the STPSat-3 platform, which was attributed to the presence

of active power systems. Therefore, while the basis of the charging arguments in [7] may not be valid, their conclusions are potentially relevant in the modern space context.

To date, the experimental investigation by Knechtel and Pitts [1] remains one of the only attempts to directly quantify the charged drag forces on LEO objects in a ground-test facility. Consequently, it represents the only currently available data to benchmark numerical methods against and establishes their ability to quantify the significance of ionospheric aerodynamic forces[1]. The purpose of this work is to compare the experimental results and conclusions made in [1] with numerical predictions made by the hybrid Particle-in-Cell (PIC)/Direct Simulation Monte Carlo (DSMC) code, pdFOAM [16]. The aim being to develop confidence in confidence in the ability of pdFOAM to reproduce charged aerodynamic trends; provide new insights into underlying physical phenomena; and, outline requirements for future experimental investigations.

CHARGED DRAG MECHANISMS

Figure 1 illustrates the general structure of negatively charged LEO plasma-body interactions. The structural complexities shown in Figure 1 are largely driven by a hyper-thermal ion ($v_{t,i}$) and sub-thermal electron ($v_{t,e}$) flow velocities relative to an orbital velocity (v_B) of $\approx$ 7.5 km/s [17]. The ion void in the wake resulting from the hyper-thermal ion flow is populated by the sub-thermal electrons, causing a negative space-charged disturbance. This space-charge disturbance results in an elongation of the wake sheath, while the directed ion velocity compresses the fore-body plasma sheath surrounding the body. It is both the existence of, and deformation of, the plasma sheath (and by extension electric field) by ion kinetic structures that underpins the exchange of momentum between the plasma and body.

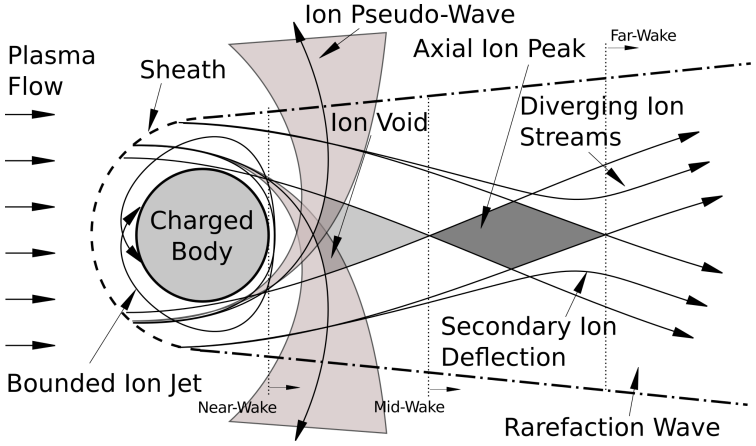

FIGURE 1. Illustration of mesothermal plasma-body interaction phenomena [18]

This momentum exchange can be accounted for by applying a control surface approach to the system, separating charged aerodynamics forces into *"direct"* and *"indirect"* components [19, 20, 21]. The main result is that, assuming a steady-state system and neglecting the electron pressure, the net charged force ($\mathbf{F_C}$) on the body can be written as,

$$\mathbf{F}_C = -\underbrace{\int_S n_i m_i \left(\mathbf{v}\cdot\hat{\mathbf{n}}\right)\mathbf{v}dS}_{\text{direct force}} + \underbrace{\int_S \bar{\mathbf{T}}\cdot\hat{\mathbf{n}}dS}_{\text{indirect force}} \tag{1}$$

where m_i is the ion mass, $\mathbf{v}$ the flow velocity vector, $\hat{\mathbf{n}}$ the outward pointing unit vector of the surface S and $\bar{\mathbf{T}}$ is the Maxwell stress tensor,

$$\bar{\mathbf{T}}_{ij} = \epsilon_0\left(E_iE_j - \frac{1}{2}\delta_{ij}E^2\right) + \frac{1}{\mu_0}\left(B_iB_j - \frac{1}{2}\delta_{ij}B^2\right) \tag{2}$$

where $E_{i,j}$ and $B_{i,j}$ is the electric and magnetic field component of the the ij element of $\bar{\mathbf{T}}$, δ_{ij} is a Kronecker delta [22], and ϵ_0 and μ_0 are the permittivity and permeability of free space respectively.

[1]It is important to note that dusty (complex) plasma experiments represent another potentially useful data source.

In summary, the expansion of the plasma sheath tends to increase the effective collection area of the body and direct charged aerodynamics forces. The thickness of the sheath combined with the sensitivity of incident ions to potential disturbances limits the expansion of this effective collection area - this is the basis of Orbital Motion Limited (OML) theory [23]. The elongation of the sheath structure caused by the directed ion velocity, however, leads to additional ion orbits not captured by OML theory, where bounded ion jets may contribute to localised direct charged forces on a body's surface. Ions deflected on these orbits but not collected contribute to indirect forces. The indirect contribution can be complex. For example, ions accelerated through the fore-body sheath and may cause a net indirect thrust on the body. This thrust must be modelled to account for the increase in apparent drag force on the fore-body caused by the accelerated ions. Ions deflected into the wake will similarly contribute a drag force as their velocity in the flow direction is reduced by the body. A more detailed discussion of the coupling of indirect and direct charged drag forces can be found in [24].

REVIEW OF EXPERIMENT AND NUMERICAL SETUP

Apparatus

Figure 2 shows the experimental setup used by Knechtel and Pitts [1] to investigate charged drag forces. Knechtel and Pitts [1] claimed to have produced a *"broad beam of singly ionized mercury plasma with a directed ion velocity range from* 8×10^8 *cm/s (or about earth-satellite velocity) up to about twice that value"* - the Authors believe that this should read 8×10^5 cm/s (8 km/s). Mercury ions were formed by bombardment with electrons from a mercury-arc discharged, accelerated to the desired energy by a biased grid and space-charge neutralised by electrons from a hot tungsten filament. The usable beam core (5 cm diameter) was claimed to have an ion density of "*about* 10^8 ions/cm^{-3}" [1]. Chamber background pressure is quoted to have been kept *"sufficiently low"* [1] to ensure free molecular flow. Spherical models (described as conducting, material not listed) with radii of 9.5 mm and 12.5 mm were mounted on a null-type quartz-fibre micro-balance sensitive from three micrograms up to several hundred micrograms of force was said to have been measured [1]. The experiment involved measuring charged drag forces for different combinations of surface potential and ion energies for the two test models.

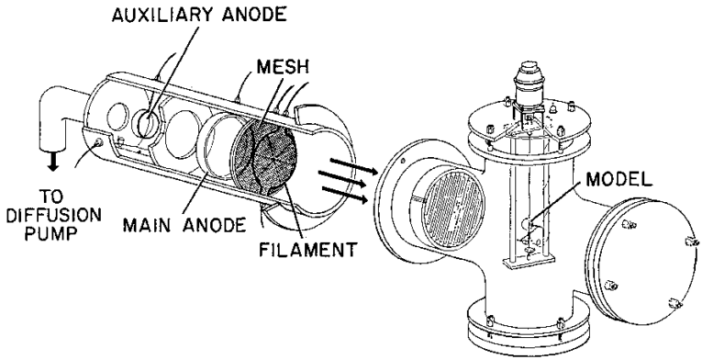

FIGURE 2. Experimental setup used by Knechtel and Pitts [1]

Based on this description, insufficient information is available to reproduce test conditions in [1] with complete confidence. Most importantly, qualitative statements regarding ion number density and chamber back pressure lead to uncertainties in the flow experienced by the test bodies. The procedure of replacing the hot tungsten filaments, which burn down with use and produce differing electron number densities, throughout the campaign is not described. Therefore, to capture the possible variations in ion number density, ion number densities of $[1, 2, 3] \times 10^{14}$ m^{-3} are considered here. Additional assumptions are made that: only singly ionised mercury ions were present with no charge exchange products; ion energies and sphere potentials were accurately controlled. Table 1 provides a summary of the test conditions considered in this work.

TABLE 1. Test conditions considered in this work based on [1].

T_i (K)	3000
T_e (K)	32810
v_B (m/s)	10000
r_B (m)	$0.0125, 0.095$
n_i (m^{-3})	$1 \times 10^{14}, 2 \times 10^{14}, 3 \times 10^{14}$
ϕ_B (V)	$0, -52.5, -105, -210, -315$

TABLE 2. Comparison of plasma-body scaling parameters.

	Knechtel and Pitts [1]	Capon, Brown, and Boyce [18]
Energy Ratio	$\frac{2q_e\phi_B}{m_i v_B^2}$	$\alpha_i = \frac{Z_i q_e \phi_B}{m_i v_B^2}$
Shielding Ratio	$R = \frac{r_B}{\lambda_{D,e}}$	$\chi = \frac{r_B}{\lambda_\phi}$
Boltzmann Coeff	$\Phi = \frac{q_e\phi_B}{k_B T_e}$	$\mu_e = \frac{q_e\phi_B}{k_B T_e}$
Speed Ratio	-	$S_i = \frac{v_B}{\sqrt{2k_B T_i/m_i}}$
Coupling Ratio	-	$\beta_i = \frac{Z_i n_i}{\sum_k^K Z_k n_k}$
Temporal Parameter	-	$\Omega_i = \frac{\omega_i r_B}{v_B}$

Scaling Relationships

Understanding scaling relationships is essential in ground test facilities, where exact operational conditions are difficult (if not impossible) to replicate precisely. Through the non-dimensionalisation of the Poissons equation with a Boltzmann electron fluid, Knechtel and Pitts [1] determined a set of three parameters that describe plasma-body interactions. Similarly, Capon, Brown, and Boyce [18] determined the set scaling relationships that define the interaction of a collisionless, multi-species, multiply charged plasma with a body at an arbitrary surface potential with respect to a quasi-neutral freestream plasma through the non-dimensionalisation of the Vlasov-Poisson system of equations and compared this with a first principles Buckingham Pi analysis and verified through self-similar PIC simulations.

Table 2 compares the scales relationships in [1] and [18] [2]. A key difference between the scaling parameters shown in Table 2 is the use of the electron Debye length $\lambda_{D,e}$ and the shielding ratio λ_ϕ in the shielding ratio χ. These length scales are written as,

$$\lambda_{D,e} = \sqrt{\frac{\epsilon_0 k_B T_e}{q_e^2 n_e}}, \quad \lambda_\phi = \sqrt{\frac{\epsilon_0 \phi_B}{q_e \sum_k Z_k n_k}} \tag{3}$$

where q_e and q_k are electron and ion charge, and k_B is the Boltzmann constant.

Physically, $\lambda_{D,e}$ describes the distance required to electrostatically shield an ion in a plasma. $\lambda_{D,e}$ implicitly applies the assumptions $q_e\phi_B \ll k_B T_e$ and $T_i \ll T_e$ and breaks down for high-voltage plasma-body interactions. [18] argues that the shielding length λ_ϕ is a more appropriate shielding length as it captures the variation of sheath thickness with surface potential and becomes $\lambda_{D,e}$ under the above assumptions. The use of $\lambda_{D,e}$ then has a significant impact on the interpretation of results in [1], where ϕ_B was used to scale α but also scaled phenomena governed by χ and μ_e.

[2] Note that q_e is an electron's charge here as opposed to a fundamental charge unit as in [18]. q_e must be written as $-q_e$ in the latter case.

Numerical Setup

Simulations were performed using the PIC portion of PIC-DSMC code, pdFOAM [16]. The cases studied are in the free-molecular regime (the mean free path $O(km)$ is much greater than model radii $O(mm)$). Hence, the DSMC portion of pdFOAM was not applied. Figure 3 illustrates the computational setup used in this work. Simulation parameters were based on those listed in Table 1, where ϕ_B was calculated to give α values similar to those considered in [1].

Simulations were of quarter-domain 3D spheres with radii of 9.5 mm and 12.5 mm and applied a hybrid fluid-kinetic approach for computational efficiency where a non-linear Boltzmann electron fluid modelled the electron distribution. Gas-surface interactions were assumed to be diffusely reflecting and neutralising with complete thermal accommodation to a 300 K wall. Wall temperature was observed to have a minor effect on drag predictions compared to charged effects but is outside the scope of this work for a detailed investigation - no wall temperature was provided in [1]. The simulation time step (δt) was 1×10^{-8} s and was chosen such that it both resolves ion oscillations defined by the ion plasma frequency $\omega_{p,i}$ ($\delta t < \omega_{p,i}/2$), and ensures that simulated ions spend multiple timesteps within a single cell $\delta t < \delta x/v$ - the latter being the limiting requirement.

Direct charged drag forces caused by gas-surface interactions were calculated from the change in momentum before and after a macro-particle collides with a body's surface. Indirect forces were calculated as the surface integral of the Maxwell stress tensor as in Eq. 1 [19, 20, 21]. The sum of direct and indirect drag forces gives the net charged drag ($F_{D,C}$).

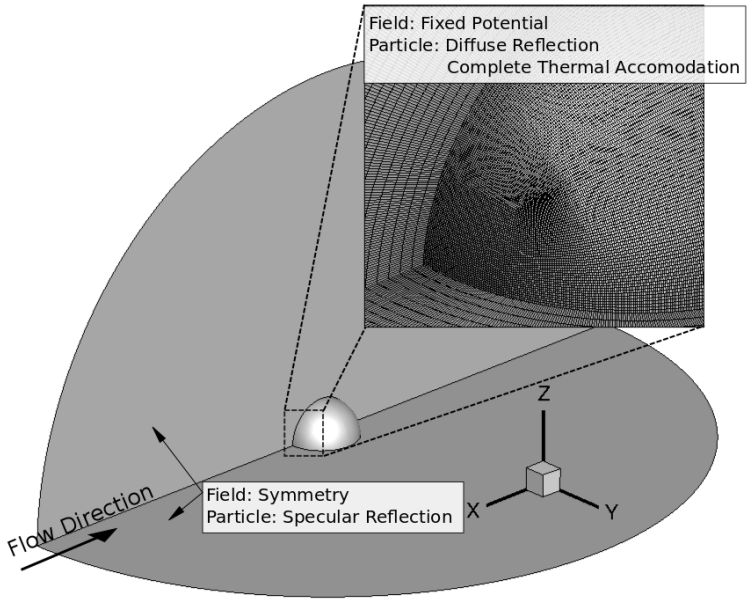

FIGURE 3. Mesh topology and boundary conditions.

RESULTS AND DISCUSSION

Based on simulation results, an object held at 0 V with respect to the surrounding plasma experiences approximately the same drag as an object in an equivalent neutral flow. Hence, from an experimental perspective, the drag on a grounded model can be approximated as the neutral drag experienced by a body in an equivalent flow if chemical effects are discounted. This finding is consistent with those in [25] and provides a basis for analysing the relative increase in charged drag compared to neutral caused by changing scaling parameters.

Figure 4 compares the experimental and numerical predictions for the variation of $F_{D,C}/F_{D,N}$ with 2α on spheres with radii of 12.5 mm (left) and 9.5 mm (right). 2α is shown to be consistent with the scaling employed in [1]. Measurements made in [1] are included in both figures to emphasise the increase in $F_{D,C}/F_{D,N}$ with decreasing radius. Figure 4 demonstrates that pdFOAM has reproduced the trend of increasing $F_{D,C}/F_{D,N}$ with increasing $-\phi_B$

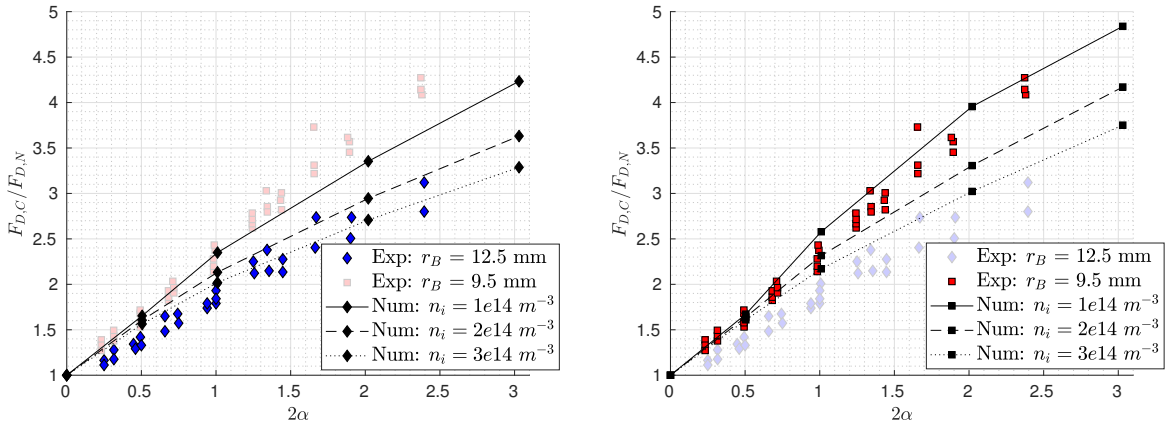

FIGURE 4. Variation of $F_{D,C}/F_{D,N}$ in α: $r_B = 12.5mm$ (left), $r_B = 9.5mm$ (right). Comparison between Experimental [1] (Exp) and numerical (Num) results.

and decreasing r_B. Numerical results in Figure 4 also highlight the sensitivity of $F_{D,C}/F_{D,N}$ to n_i. Given the uncertainty in n_i, a quantitative comparison between numerical and experimental results is difficult. Instead, we shall focus on investigating the underlying cause of these trends.

Knechtel and Pitts [1] hypothesised that the increase in $F_{D,C}/F_{D,N}$ with decreasing r_B was caused by an increase in forces from "non-impacting ions" i.e. indirect forces. Figure 5 tests this conclusion by separating the net direct ($C_{D,d}$) and indirect ($C_{D,m}$) drag coefficients predicted by pdFOAM and plotting the relative increase between the 9.5 mm and 12.5 mm radius spheres e.g. $\Delta C_{D,d} = C_{D,d}(r_B = 9.5mm) - C_{D,d}(r_B = 12.5mm)$.

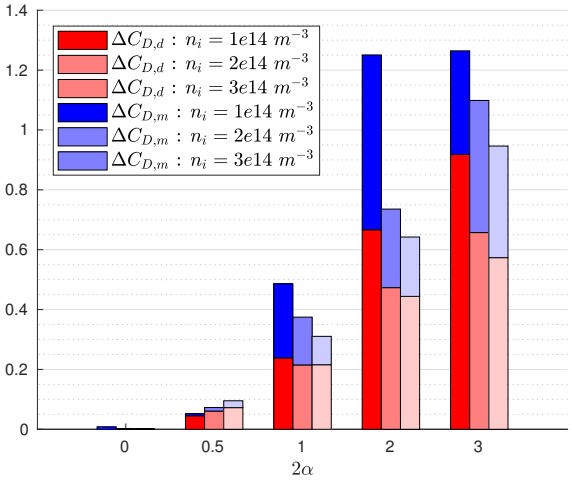

FIGURE 5. Relative contribution of direct ($C_{D,d}$) and indirect ($C_{D,m}$) drag effects on the 9.5 mm vs 12.5 mm model.

Figure 5 illustrates that, for all n_i considered, the primary cause for increasing $F_{D,C}/F_{D,N}$ for the 9.5 mm sphere relative to the 12.5 mm sphere was due to direct charged drag forces (red bars). Figure 5 also shows that indirect effects became increasingly important with increasing sheath thickness (increasing $-\phi_B$ and decreasing r_B). This is particularly evident in the 1×10^{14} m^{-3} cases, where the indirect force on the $\alpha = 2$ was 68% greater than the $\alpha = 3$ case. This non-linear behaviour was not seen for the 2×10^{14} m^{-3} and 3×10^{14} m^{-3} cases, where both indirect and direct forces increased monotonically with $-\phi_B$ suggesting a transition occurred in the underlying physics between the 1×10^{14} m^{-3} and 2×10^{14} m^{-3} cases. A detailed investigation of this behaviour is beyond the scope of this work.

Comparing the trends in Figure 5 with the conclusion in [1] that indirect effects caused the increase in $F_{D,C}/F_{D,N}$ with decreasing radius, we conclude instead that the primary source of the rise is likely due to direct charged aerodynamic effects. Based on the shielding ratio in Table 2, we conjecture that the reason for the increase is related to the increase in relative sheath thickness.

A drawback of the shielding ratio employed in [1] is the use of the electron Debye length $\lambda_{D,e}$ as a proxy for sheath thickness. While $\lambda_{D,e}$ captures the electrostatic shielding of an ion in a plasma, it does not capture the variation of sheath thickness with ϕ_B as $\phi_B \gg k_B T_e/q_e$. Therefore, as the surface potential of the test models increases, the thickness of the sheath surrounding both models increases - this behaviour is studied in detail in [24]. Consequently, the effective collection area (direct forces) and the number of deflected ions (indirect forces) increased on both models. The relative thickness of the sheath, however, was greater for the smaller model for the same ϕ_B increasing $F_{D,C}/F_{D,N}$ compared to the larger model. This behaviour is captured in Figure 6, which plots $F_{D,C}/F_{D,N}$ against χ^{-1}. A clear linear relationship between $F_{D,C}/F_{D,N}$ and both r_B and n_i is observable for a given ϕ_B. An interesting feature of Figure 6 is the gradient of this linear relationship for given ϕ_B. Unfortunately, the coupling of ϕ_B with α, χ and μ_e (not investigated here), makes it difficult to determine the physical phenomena driving this feature.

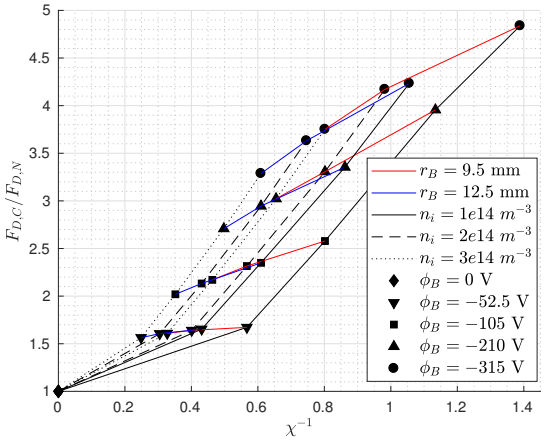

FIGURE 6. Variation of $F_{D,C}/F_{D,N}$ in χ^{-1}.

Overall, the above discussion has demonstrated the ability of pdFOAM to capture trends in $F_{D,C}/F_{D,N}$ and highlighted the sensitivity of results to uncertainties in n_i. The coupling of α, χ and μ_e with the primary test parameter ϕ_B in [1] also made it difficult to determine the underlying phenomena governing the observed changes in $F_{D,C}/F_{D,N}$. Principle recommendations of this work for future experiments are therefore careful characterisation of ion sources and to design experiments where the effects of scaling parameters can be investigated independently.

CONCLUSIONS

The evolving nature of the challenges facing LEO activities requires advances in space traffic management capabilities that are contingent on an understanding of all the forces affecting a body's motion. The aerodynamic interaction of LEO objects with the ionosphere (ionospheric aerodynamics) is currently not considered. This work presented a review of the early charged drag experiment performed by Knechtel and Pitts [1] and comparisons with predictions made using the PIC-DSMC code, pdFOAM. While uncertainties in the experimental description made an accurate reconstruction of the results in [1] difficult, the following observations were made: pdFOAM was successfully able to reproduce trends observed experimentally in [1]; scaling of plasma-body interactions must be able to account for artificial body potentials; the design of experiments should carefully consider the coupling of phenomena if using body potential as a test parameter; and the increase in charged drag forces on the small test model studied by Knechtel and Pitts [1] may have been primarily caused by an increase in relative sheath thickness (and direct drag forces) instead of indirect effects as previously hypothesized.

ACKNOWLEDGMENTS

This research was undertaken with the assistance of resources from the National Computational Infrastructure, which is supported by the Australian Government. This material is based upon work supported by the Air Force Office of Scientific Research award FA2386-17-1-4105.

REFERENCES

[1] D. Knechtel and W. C. Pitts, AIAA Aerospace Sciences Meeting **2**, 1148–1151 (1965).
[2] E. Doornbos and H. Klinkrad, Advances in Space Research **37**, 1229–1239 (2006).
[3] K. Moe and M. M. Moe, Planetary and Space Science **53**, 793–801 (2005).
[4] D. A. Vallado and D. Finkleman, Acta Astronautica **95**, 141–165 (2014).
[5] C. L. Brundin, AIAA Journal **1**, 2529–2538 (1963).
[6] G. Cook, Planetary and Space Science **13**, 929–946 (1965).
[7] R. Jastrow and C. A. Pearse, Journal of Geophysical Research **62** (1957).
[8] P. J. Wyatt, Journal of Geophysical Research **65**, 1673–1678 (1960).
[9] K. P. Chopra and S. F. Singer, Heat Transfer and Fluid Mechanics Institute (1958).
[10] K. P. Chopra, Review of Modern Physics **33** (1961).
[11] E. C. Whipple, Reports on Progress in Physics **44**, 1197–1250 (1981).
[12] H. B. Garrett, Review of Geophysics **19**, 577–616 (1981).
[13] H. B. Garrett and A. C. Whittlesey, IEEE Transactions on Plasma Science **28**, 2017–2028 (2000).
[14] D. E. Hastings, Journal of Geophysical Research **100**, 14457–14483 (1995).
[15] G. McHarg, P. Neal, N. Taormina, A. Strom, and R. Balthazor, Space Weather **13**, 827–830 (2015).
[16] C. J. Capon, M. Brown, C. White, T. J. Scanlon, and R. R. Boyce, Computers and Fluids **149**, 160–171 (2017).
[17] N. H. Stone, "The Aerodynamics of Bodies in a Rarefied Ionized Gas with Applications to Spacecraft Environmental Dynamics," Tech. Rep. (Marshall Space Flight Center, Alabama, 1981).
[18] C. J. Capon, M. Brown, and R. R. Boyce, Physics of Plasmas **24** (2017), 10.1063/1.4979191.
[19] C. J. Capon, M. Brown, and R. R. Boyce, Advances in Space Research **62**, 1090–1101 (2018).
[20] J. E. Allen, Journal of Plasma Physics **73**, 773–783 (2007).
[21] I. H. Hutchinson, Plasma Physics and Controlled Fusion **47**, 71–87 (2004).
[22] F. P. Miller, A. F. Vandome, and M. John, *Maxwell Stress Tensor* (VDM Publishing, 2010).
[23] J. E. Allen, Physica Scripta **45**, p. 497 (1992).
[24] C. J. Capon, "Ionospheric Aerodynamics in Low Earth Orbit," Ph.D. thesis, University of New South Wales Canberra 2017.
[25] C. A. Maldonado and A. D. Ketsdever, 53rd AIAA Aerospace Sciences Meeting (2015), 10.2514/6.2015-1392.
[26] É. Choinière and B. E. Gilchrist, IEEE Transactions on Plasma Science **35**, 7–22 (2007).
[27] I. H. Hutchinson, Plasma Physics and Controlled Fusion **48**, 185–202 (2006).
[28] K. P. Chopra, Review of Modern Physics **33** (1961).
[29] D. F. Hall, R. F. Kemp, and J. M. Sellen, AIAA Electric Propulsion Conference **2**, 1032–1039 (1964).

Appendix B

Experimental Investigation of Ionospheric Aerodynamics Effects

(Peer-reviewed conference paper from the 31st Symposium on Rarefied Gas Dynamics in AIP conference proceedings.)

Experimental Investigation of Ionospheric Aerodynamics Effects

P. Lorrain[1,a)], C. J. Capon[1], R. R. Boyce[1], C. A. Maldonado[2] and A. D. Ketsdever[3]

[1]*University of New South Wales Canberra, Canberra, ACT 2610, Australia.*
[2]*Imprimis, Inc., Colorado Springs, CO 80903, United States*
[3]*Oregon State University Cascades, Bend, OR 97702, United States*

[a)]Corresponding author: p.lorrain@unsw.edu.au

Abstract. The accurate prediction of the motion of resident space objects (RSOs) in Low Earth Orbit (LEO) requires knowledge of all forces acting on these objects, which includes active and inactive (e.g. debris) objects. In this context, charged particle interactions with RSOs and associated orbital perturbations resulting from charged aerodynamic effects, i.e. momentum exchange between the ambient plasma and the RSO, are currently poorly understood and typically neglected. This paper presents results from an experimental investigation aimed at quantifying the net force imposed on a charged test object subjected to a 5 eV streaming Ar^+ plasma representative of the plasma-body interaction experienced by RSOs orbiting within the ionosphere in LEO. In addition to net charged force measurements, the ion current collected by the charged test object was recorded. An increase in force with increasing negative test object surface potential was measured, in accord with numerically predicted behavior. Differences in the trends for the force and current measurements were observed with increasing negative test object surface bias. This can be attributed to indirect ion momentum exchange resulting from the electrostatic interaction between the streaming ions and the electrostatic sheath surrounding the charged test object. This indirect force acts to reduce the direct charged force (from ions hitting the surface) imparted on the charged test object. Numerical reconstruction of the experiments using an in-house PIC code showed very good good agreement with the experimental current data but could not accurately resolve the trend for the net charged forces with increasing test object surface bias. Further work is currently ongoing to understand and resolve this discrepancy.

INTRODUCTION

Space-based technology is an integral enabler for modern society, providing essential services for weather monitoring and prediction, disaster and emergency management, environmental monitoring, navigation, telecommunication, and defence and national security. As a consequence, Low Earth Orbit (LEO) is becoming increasingly crowded with an ever-growing number of spacecraft launched into orbit around our planet. In addition, space debris, e.g. defunct spacecraft or fragments of spacecraft originating from collisions, poses a serious threat to active spacecraft, and the US Air Force Space Command issues daily warnings of possible collisions to spacecraft operators. This situation demands an increase in Space Situational Awareness capabilities worldwide with regard to orbit determination and prediction capability [1]. Alongside advances in space surveillance, a key requirement is an improved understanding of the underlying physics that govern the interaction of orbiting spacecraft with the environment they are immersed in.

Spacecraft in LEO experience a complex interaction with the neutral and plasma environment in the ionosphere [2]. At LEO altitudes, orbiting spacecraft interact with the rarefied charged particle environment of the ionosphere which exists because of solar radiation induced photo-dissociation processes of the molecules in the upper layers of the atmosphere. The dominant species in the altitude range above 200 km are singly charged atomic oxygen ions (O^+) and at (even) higher altitudes singly charged atomic hydrogen (H^+) ions, which impact RSOs in LEO at orbital velocity of approximately 7.5 km/s. As described below, such ionospheric aerodynamic effects can potentially magnify the aerodynamic effects of neutral particle impacts [3, 4, 5, 6].

Today, the drag of orbiting spacecraft represents one of the largest sources of error for orbit determination [7]. Spacecraft drag in LEO due to interactions with the residual neutral atmosphere has been studied in detail, and significant reductions in uncertainties of spacecraft drag coefficients can be attributed to an improved understanding and

modeling of gas-surface interactions [8, 9]. However, the electrostatic interaction of the orbiting spacecraft with respect to aerodynamic effects, i.e. charged aerodynamics, has traditionally not been given much attention, a result of early work by Brundin [10]. Brundin concluded that drag due to charged particle interactions may be neglected compared to neutral aerodynamic effects due to the low natural body floating potentials adopted by RSOs in LEO, and for decades the international space community followed that conclusion. Thus the effects of charged particle interactions on LEO spacecraft motion are less well understood. Brundin's conclusion is likely no longer valid however, as modern spacecraft have evolved into inherently more complex systems which typically incorporate high voltage power systems, such as solar panels or electric or plasma propulsion systems, resulting in potentially much larger spacecraft surface potentials [2]. As an example, the authors in [11] state measured spacecraft floating potentials between -25 V and -35 V for the STPSat-3 cubesat in a 500 km circular orbit with an inclination of 40.5°. In addition to this, spacecraft passing through high latitude and the polar auroral zones experience increased levels of surface charging due to interaction with high energetic precipitating particles [2].

Recently, Capon et al. [4, 5, 6] have provided a comprehensive investigation of charged aerodynamics effects relevant to LEO spacecraft by means of numerical simulations of the ionospheric plasma-body interaction for a two-dimensional cylinder geometry. Their research presents a new, physics-based framework for modeling and understanding plasma-body interactions through the development of appropriate scaling laws for ionospheric plasma-body interactions, which takes into account the effect of arbitrary, potentially large, surface potentials of LEO spacecraft [6]. The numerical work presented in [4, 5] shows that depending on the surface potential of the object and the ratio of charged to neutral particle densities in the freestream, charged aerodynamics can be significant compared to neutral aerodynamics. In particular at higher LEO altitudes, where charged particle interactions occur more frequently than neutral particle interactions, charged drag was found to outweigh neutral drag. Their research has further revealed the important result that with increasing negative surface potential the plasma-body interaction can yield ion thrust forces which partially mitigate charged drag effects. The important missing piece of the puzzle is a benchmark-quality experimental investigation of these charged aerodynamic phenomena.

The only relevant published ground-based experimental work attempting to quantify charged drag forces for a LEO like plasma-body interaction was conducted by Knechtel and Pitts [12]. Knechtel and Pitts exposed two different size sphere test objects (radii of 0.095 m and 0.0125 m) to a streaming mercury plasma for a range of negative test object surface potentials. The induced force from charged particle momentum exchange was then measured using a null-type quartz-fiber micro-balance sensitive from three micro-grams up to several hundred micro-grams of force [12]. Charged drag measurements were presented in terms of charged-to-neutral force ratios (the neutral component taken as the force measured for a grounded test object), demonstrating a measurable force increase with increasing negative test object surface potential. However, insufficient information was provided regarding the details of the test setup and the actual test conditions to allow for a faithful reproduction of these experiments, either experimentally or numerically, and to provide confidence in the experimental data and gain insight into the underlying physics governing the observed trends.

The purpose of this work is to develop a coupled experimental and numerical approach for fundamental studies of charged aerodynamics in the LEO context. The approach adopted here follows best practice aerospace R&D applied to space physics, where progress in the science of aerodynamics (including ionospheric aerodynamics) is achieved through coupling numerical simulations with experimental measurements. The experiments, while not precisely replicating the actual flow conditions, nevertheless contain the relevant physical processes provided care is taken in observing the relevant scaling parameters when planning and setting up the tests. Numerical simulations are validated by the experimental measurements and enable the key physical phenomena to be understood in detail. This paper presents results from preliminary experimental efforts complemented by numerical reconstructions of the experiments.

IONOSPHERIC AERODYNAMICS PHENOMENA

The plasma-body interaction experienced by RSOs orbiting in the ionosphere in LEO is characterized by an unequal ion and electron flux which is due to the high orbital velocity of the orbiting object, of order 7.5 km/s, and the large difference between ion and electron thermal velocities due to their large difference in mass. To counteract the imbalance in ion and electron fluxes and achieve an equilibrium state, where the ion current equals the electron current to the body, objects in LEO tend to attain a negative surface potential. In addition, the high relative kinetic energy between the ions and orbiting objects of approximately 5 eV creates a myriad of complex plasma-body interaction phenomena, which are illustrated schematically in Fig. 1 [5]. This interaction is referred to as ionospheric aerodynamics for the

remainder of this paper. A highly distorted sheath structure develops around the charged object. On the ram facing side, the sheath is compressed due to the hyper-velocity impact of ions. On the wake side, the sheath is elongated due to an ion void or negative space-charge region that forms immediately behind the object. The ion void is a result of the faster moving electrons being able to populate the region behind the object more easily than the slower moving ions. Ion motion is subsonic with respect to the orbiting body whereas the electrons travel supersonically with respect to the orbiting body, a condition known as meso-thermal flow. An increase in surface charge of an object results in

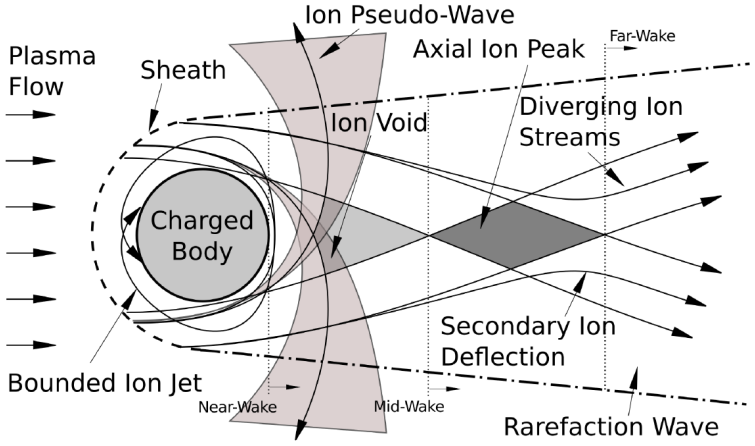

FIGURE 1. Schematic illustration of ionospheric aerodynamics phenomena [5].

an expansion of the sheath surrounding it, thereby causing the electrostatic disturbance to extend further out into the ambient plasma environment. This results in a growing effective capture area for ions and a stronger electrostatic interaction between the ions and the object, i.e. ions getting deflected into larger angles around the object.

The complex sheath structure and associated ion kinetics result in direct and indirect charged forces exerted onto an object immersed in a meso-thermal streaming plasma. Direct charged forces are driven by momentum exchange due to ions impacting the objects surface. Indirect charged forces result from momentum exchange due to ions being deflected around, but not collected by, the object within the electrostatic disturbance (sheath) surrounding the object. On the ram side, the acceleration of ions in the forebody sheath results in a thrust contribution, whereas the ion deflection into the wake and associated reduction in the streamwise velocity component causes a drag contribution to the overall force balance on the object. This discussion highlights the importance of including both direct and indirect forces in the investigation of the effect of ionospheric aerodynamics on the motion of RSOs. A detailed discussion of the complex coupling between direct and indirect charged forces can be found in [5, 13].

The momentum exchange between charged particles and a charged object, accounting for both direct and indirect mechanisms, can be determined by applying a control surface approach to the system. The development of this approach for meso-thermal LEO plasma-body interaction is described in detail in [5]. Assuming steady-state and neglecting the electron pressure, the total (net) charged force, $\mathbf{F_C}$, on an object in a meso-thermal plasma flow is defined as

$$\mathbf{F_C} = -\underbrace{\int_S n_i\, m_i (\mathbf{u}\cdot\hat{\mathbf{n}})\, dS}_{\text{direct force}} + \underbrace{\int_S \overline{\mathbf{T}}\cdot\hat{\mathbf{n}}\, dS}_{\text{indirect force}}, \tag{1}$$

where n_i and m_i are the ion number density and mass, respectively, $\mathbf{u}$ is the streaming ion velocity vector, $\hat{\mathbf{n}}$ is the outward pointing surface unit vector, S is the control surface and $\overline{\mathbf{T}}$ is the Maxwell stress tensor describing the indirect momentum exchange due to the electrostatic interaction of the ions with the charged object. The Maxwell stress tensor is given as

$$\overline{\mathbf{T}}_{ij} = \epsilon_0 \left(E_i\, E_j - \frac{1}{2}\delta_{ij}\, E^2 \right) + \frac{1}{\mu_0}\left(B_i\, B_j - \frac{1}{2}\delta_{ij}\, B^2 \right), \tag{2}$$

where E_{ij} and B_{ij} are the electric and magnetic field components of $\overline{\mathbf{T}}_{ij}$, δ_{ij} is the Kronecker delta, and ϵ_0 and μ_0 are the vacuum permittivity and permeability, respectively. The reader is referred to [5] for a detailed derivation of the equations.

The ability to accurately reproduce LEO plasma-body interactions in a ground-based test facility requires the generation of a plasma flow, representative of LEO plasma characteristics, past a stationary test object inside a vacuum chamber, forming a plasma/ionospheric wind tunnel. An important part of any ground-based experimental research is an understanding of the relevant scaling parameters for the physical problem under consideration to guarantee representative test conditions. Through dimensional analysis applied to the governing equations for LEO plasma-body interactions - the collision-less Boltzmann (Vlasov) equation and Poisson's equation with a Boltzmann electron fluid - Capon et al. [6] derived and applied a generalized set of scaling laws that describe meso-thermal plasma-body interactions to map out key physical phenomena that influence ionospheric aerodynamic forces. Their research identified two key dimensionless parameters shown to govern the ionospheric aerodynamic behavior, given in Eqn. 3 and 4,

$$\alpha = \frac{q_e \, \Phi_B}{m_i \, v_i^2}, \qquad \text{ion deflection parameter} \tag{3}$$

$$\chi = \frac{r_B}{\lambda_\Phi}, \; \lambda_\Phi = \left(-\frac{\epsilon_0 \, \Phi_B}{q_e \, \Sigma_i \, n_i} \right)^{1/2}, \qquad \text{general shielding ratio} \tag{4}$$

where Φ_B is the object surface potential, q_e is the elementary charge, ϵ_0 is the vacuum permittivity, r_B is a characteristic object dimension (e.g. the radius of a spherical object), and m_i, v_i and n_i are the ion mass, streaming velocity and number density, respectively.

The ion deflection parameter physically represents the ratio of ion potential and kinetic energy. It is effectively a measure of how strongly ion trajectories are affected by the electric field that builds up around a charged object. The general shielding ratio describes the relative size of the sheath compared to a characteristic object dimension. For small χ or large values of χ^{-1} the object is weakly shielded, i.e. the sheath is large compared to the size of the object, and thus electrostatic effects potentially play a significant part in the plasma-body interaction and the charged force distribution imposed on the object. An increase in an object's surface potential causes an increase in both α and χ^{-1} values indicating a significant influence on ion kinetic behavior and thus charged forces.

Through careful application of the scaling framework developed by Capon et al. [6] a ground-based investigation of ionospheric aerodynamics, applicable to full-scale orbital flight, is possible. The work presented in this paper represents a significant step towards establishing a state-of-the-art ground-based experimental ionospheric aerodynamics research capability.

EXPERIMENTAL AND NUMERICAL SETUP

Experimental Apparatus

The experiments described in this paper were conducted in the Chamber for Atmospheric and Orbital Space Simulation (ChAOSS) facility at the University of Colorado Colorado Springs (UCCS). ChAOSS is a 1 m diameter and 2.5 m long cylindrical vacuum chamber, which is capable of achieving a base pressure of 1×10^{-7} Torr using a 500 mm cryogenic pump. The facility setup is described in detail in [14].

TABLE 1. Plasma source operating conditions. The source was operated on Argon gas for all tests.

Flow Rate, $\dot{m}$ [sccm]	**Discharge Voltage,** Φ_D **[V]**	**Discharge Current,** I_D **[A]**
4	53	5.5

TABLE 2. Plasma flow conditions determined from RPA and Langmuir probe measurements.

Number Density, n_i **[m^3]**	**Electron Temperature,** T_e **[eV]**	**Streaming Ion Energy,** E_i **[eV]**	**Ion Deflection Parameter,** α **[-]**	**General Shielding Ratio,** $\chi^{-}1$ **[-]**
2 x 10^{13}	0.57	5	5.1 - 51	0.26 - 0.83

Representative LEO plasma flow conditions were simulated using a magnetically filtered plasma source developed collaboratively between the Center for Laser Energy and Exploration Research (CLEER) located at UCCS and

the Center for Electric Propulsion and Plasma Engineering (CEPPE) located at Colorado State University. The design and operation of the source are described in detail in [15, 16]. The plasma source was operated on Argon gas, at a flow rate of 4 sccm, for all experiments. To accurately replicate LEO plasma-body interaction conditions, the source operating conditions were chosen to achieve a streaming energy of the ions of ≈ 5 eV and low electron temperature, $T_e < 1$ eV, which was confirmed through retarding potential analyzer (RPA) and Langmuir probe measurements, respectively. The number density was also obtained from Langmuir probe measurements. Argon gas was chosen to eliminate complexities from surface chemistry effects that would be present if Oxygen gas was used. The plasma source operating conditions and experimental test conditions are provided in Tables 1 and 2, respectively. Plasma source properties were allowed to stabilize for approximately 20 minutes prior to taking any measurements.

It is important to note that the background pressure inside the vacuum chamber was maintained at $\leq 3\times10^{-5}$ Torr during plasma source operation, which reduced the likelihood of $Ar^+ - Ar$ charge-exchange (CEX) collisions. Resonant CEX within the plasma flow exiting the plasma source occurs when the ion-neutral mean free path for $Ar^+ - Ar$ collisions is small, which is a function of the vacuum chamber background pressure. CEX collisions cause the streaming Ar^+ ions to lose their energy to adjacent neutral Ar atoms resulting in a bi-modal ion energy distribution function (IEDF). In the extreme case, i.e. at sufficiently high vacuum chamber background pressure (approximately $\geq 1\times10^{-4}$ Torr), the bulk of the streaming ion energy is lost to neutrals and only thermal, non-streaming ions remain - a scenario to be avoided for a faithful experimental simulation of the LEO plasma flow environment. The IEDF determined from the RPA measurements for tests considered here showed only a single narrow peak representative of an accelerated ion population at ≈ 5 eV.

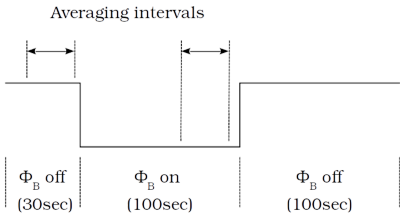

FIGURE 2. Test profile for experimental charged force measurements.

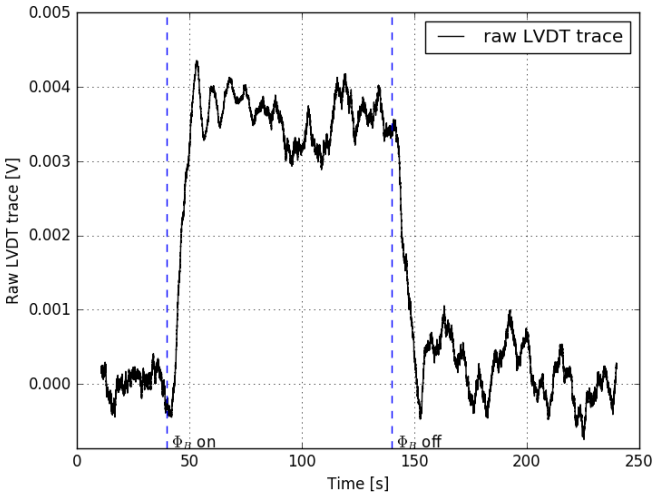

FIGURE 3. Sample LVDT trace showing sensor response to change in test object surface bias.

Charged drag measurements were conducted on a square, 88.9 mm (3.5 inch) edge length and 5 mm thick aluminium plate mounted to one end of a nano-Newton thrust stand (nNTS). The nNTS is a torsional force balance that relates linear displacement of the thrust stand lever arm, measured using a linear variable differential transformer

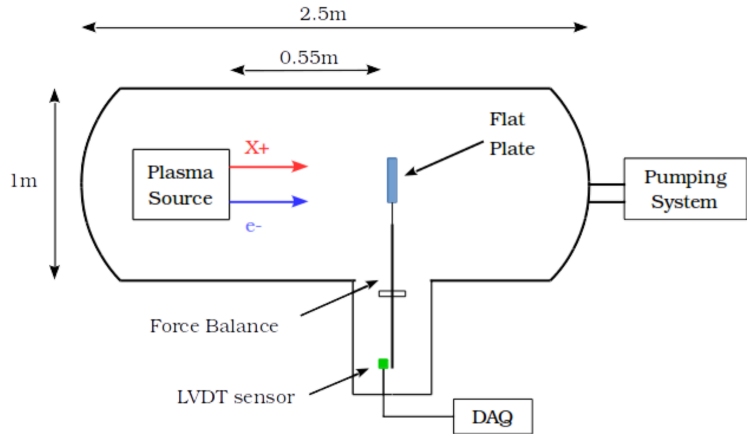

(a) Schematic of experimental setup.

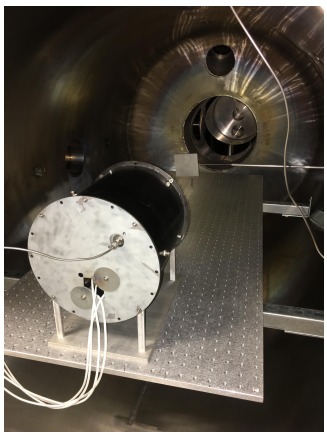

(b) Plasma source and flat plate installation inside ChAOSS facility at UCCS.

FIGURE 4. Experimental setup for charged drag experiments.

(LVDT), to a known force determined by means of an electrostatic calibration system integrated into the thrust stand setup. Force measurements with a resolution of 10 nN are possible. A detailed description of the nNTS and calibration procedure is given in [17]. The flat plate was positioned 0.55 m downstream of the plasma source exit at 90° angle of incidence to the oncoming plasma flow. Force measurements were taken for a range of test object surface biases (Φ_B) ranging from 0 V to -500 V at 50 V increments. The test profile employed for each force measurement is depicted in Fig. 2 and was as follows: test object at ground potential ($\Phi_B = 0$ V) for 30 s, surface bias turned on for 100 s, surface bias turned off (i.e. test object at ground potential again) for 100 s, so that a total of 230 s of data were recorded from the LVDT sensor for each surface bias step. Five separate measurements were taken at each surface bias step to demonstrate repeatability of results. A sample LVDT trace is shown in Fig. 3 illustrating the response of the LVDT sensor reading to a change in test object surface bias during a measurement cycle. Two 20 s averaging intervals, shown in Fig. 2, were chosen where the LVDT sensor reading had stabilized to compute integrated force values. The force data in this paper are presented in terms of charged-to-neutral force ratios defined as

$$\frac{F_C}{F_N} = \frac{F_{c\,(\Phi_B\,on)}}{F_{c\,(\Phi_B = 0\,\mathrm{V})}}. \tag{5}$$

This force ratio effectively indicates the change in force on the test object due to the electrostatic disturbance field created around it by the increase in negative surface potential. The force measured for $\Phi_B = 0$ V is considered to be equivalent to a neutral particle interaction (hence the notation F_N) where the momentum exchange occurs only on the ram face of the test object. This assumption is consistent with the findings in [18].

The ion current collected by the test object was recorded as a proxy for direct ion momentum exchange due to ions hitting the test object surface. Any differences observed in the trends between net force and collected current measurements can then be attributed to indirect momentum exchange mechanisms as described in the previous section. This measurement further aids in the verification of the PIC simulations. Surface bias control and collected current measurements were achieved using a Keithley 6487 sourcemeter.

A schematic of the experimental setup is given in Fig. 4(a), and Fig. 4(b) shows a photo of the plasma source and nNTS arm with the flat plate test object installed inside the ChAOSS facility.

Numerical Setup

Numerical reconstruction of the experimental plasma-body interaction flowfields was performed using the in-house PIC-DSMC code pdFOAM [19]. Two-dimensional half-domain and three-dimensional quarter-domain simulations were conducted for a range of negative surface potentials between 0 V and -500 V. The plasma flow freestream conditions prescribed as the inflow to the simulations are the experimental test conditions compiled in Table 2. The test object surfaces are treated as diffusively reflecting, and impacting ions are neutralized assuming complete thermal

accommodation to a 350 K wall. A fixed potential of 0 V was prescribed at the outer domain boundaries and symmetry planes were treated as specularly reflecting boundaries for the particle distribution. The simulations assume free molecular flow as the mean free path, $O(km)$, is much larger than any characteristic dimension of the test object, $O(cm)$. Consequently, the DSMC part of the code was not used in the simulations. In addition, no ion-neutral collisions were considered. The electron distribution was modeled using a non-linear Boltzmann electron fluid model. The grid resolution was chosen to be smaller than the Debye length and the time step for the simulation was fixed at $5 \times 10{-}8$ s to ensure that ions spend multiple timesteps within a single cell. Each computation included a total of ≈2 M and ≈19 M simulated charged macro particles, for the 2-D and 3-D simulations, respectively. Computations performed with twice the number of simulated particles confirmed that the numerical results were not affected by insufficient particle resolution.

Direct and indirect charged forces were calculated from the simulation data using Eqns. 1 and 2. Experimental and numerical results are compared in terms of total current collected by the test object and total, i.e. net, charged-to-neutral force ratios. As previously noted, the neutral component represents the force exerted on the grounded test object, i.e. for $\Phi_B = 0$ V. The numerical results further allow for a breakdown of total forces into direct and indirect momentum exchange contributions (see Eqn. 1), thereby providing a means to explore the physics underlying the observed experimental trends.

RESULTS AND DISCUSSION

Measurements were made to explore the change in the net charged force on a flat plate immersed in a meso-thermal plasma flow due to variations in the plate's surface potential, as described in the previous section. The ion current collected by the test object was recorded as a proxy for direct ion momentum exchange due to ions hitting the test object's surface. Any differences observed in the trends for the measured net force and collected ion current with increasing negative surface potential would then be attributable to indirect ion momentum exchange mechanisms. The latter effect is related to the electrostatic interaction between the streaming ions and the electrostatic sheath surrounding the charged test object discussed earlier in this paper.

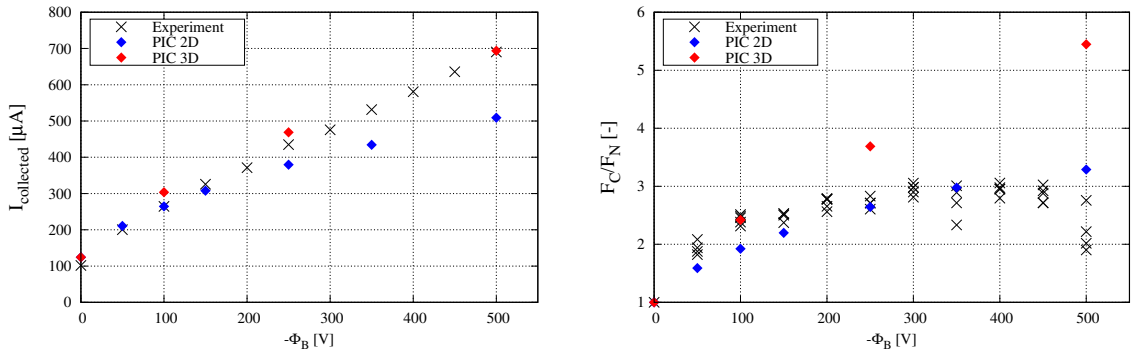

(a) Collected ion current.

(b) Charged-to-neutral force ratios.

FIGURE 5. Experimental measurements of ion current collected by the flat plate test object during the charged drag measurements and measured charged-to-neutral force ratios obtained using the nNTS. Numerical results from 2-D and 3-D PIC simulations are superimposed on the plots.

Figures 5(a) and 5(b) show the experimental results for collected current and net charged-to-neutral force ratio as a function of negative plate surface potential. The reader is reminded that the neutral force component is considered to be the force on the test object for $\Phi_B = 0$ V. The plotted current values represent the mean of five measured (integrated) current values for each surface bias step. The variation in the current measurements was less than 1 %. After an initial steep rise, the experimental current values increase monotonically with negative surface potential. This behavior is expected from the numerical simulations of Capon et al. [5], and can be explained by the expansion of the sheath around the flat plate increasing the effective collection volume for ions, drawing in more and more ions that ultimately impact on the plate surfaces. The net charged force measurements shown in Fig. 5(b) illustrate a different trend compared to the current data. The charged force on the plate increases with increasing negative

surface potential until approximately $\Phi_B = -150$ V and then levels off showing no further increase nor decrease with increasing negative surface bias. The force data for $\Phi_B = -500$ V should be interpreted with caution, as the LVDT sensor readings exhibited a significant amount of thermal drift and noise, which complicated the data processing and provided low confidence in the accuracy of the measured data. Nevertheless the data points are included here for completeness.

The different trends in the experimental current and force data suggests the existence of a counteracting force, which becomes more influential with increasing negative plate surface bias, in particular from approximately $\phi_B = -150$ V. This is consistent with the discussion provided earlier in this paper concerning indirect forces. In addition to a growing ion collection area (increasing χ^{-1}), as the sheath expands and the electric field around the object occupies and influences are larger volume, the electrostatic potential energy becomes larger and larger relative to the ion kinetic energy (increasing α). The ions react to this stronger electrostatic disturbance by being deflected into larger angles around the object causing an increase in the indirect forces. The measurements can be seen to be fairly repeatable and distinct force increments between the different surface bias steps are discernible. More force data will be collected for each test point in future experiments to allow for a detailed statistical analysis and representation of the experimental data.

Numerical results from 2-D and 3-D PIC simulations aimed at reconstructing the experimental plasma-body interaction flowfields are superimposed on the plots in Fig. 5. The net forces extracted from the 2-D simulations fall within the same range as the experimental measurements suggesting good agreement between experiments and PIC simulations, however, the collected current values show a growing deviation from the measured current data for plate surface biases larger than -150 V. The two-dimensional simulations fail to capture the sheath expansion and ion collection from the third dimension. This affects current collection on the ram facing side of the test object as well as the structure of the deflected ion trajectories behind the object and thus the resulting current flux onto the wake facing surface of the test object, as will be seen later.

The 3-D PIC simulations capture the experimental trend for the collected current measurements very well. While there is good agreement between numerical and experimental force ratios at $\Phi_B = -100$ V the numerical force ratios start to diverge from the experimental measurements for larger negative surface biases reaching almost twice the experimental value at $\Phi_B = -500$ V. The good agreement between experimental and numerical collected current values is encouraging and suggests that the current flux to the plate surfaces, and thus the net direct force on the object, is adequately captured by the 3-D PIC computations. Future experiments will include separate collected current measurements for the ram and wake facing surfaces. This will help to show direct drag and thrust contributions to aid the verification of the numerical simulations.

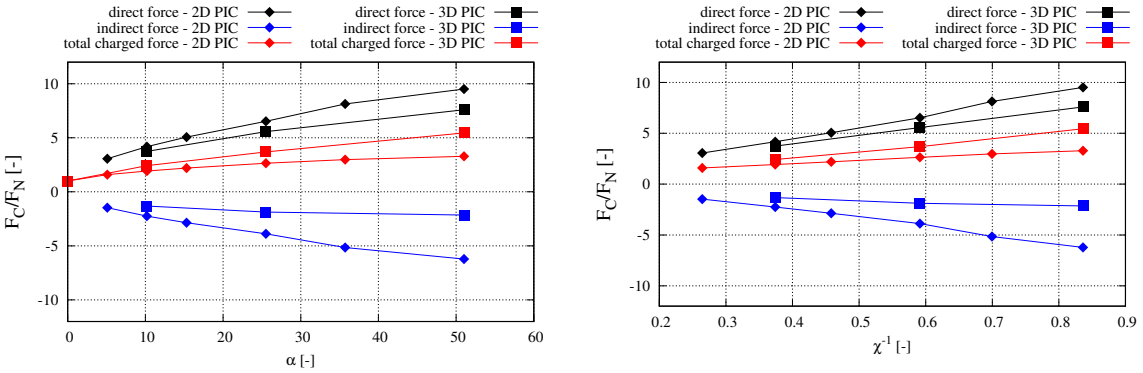

(a) α variation of force ratios.

(b) χ^{-1} variation of force ratios.

FIGURE 6. Numerical results for direct, indirect, and net charged-to-neutral force ratio as a function of α and χ^{-1}.

Figure 6 shows a breakdown of the 2-D and 3-D numerical force ratios into net direct and indirect contributions plotted as a function of α (Fig. 6(a)) and χ^{-1} (Fig. 6(b)). The traces show the expected trend of increasing direct and net charged forces with increasing α and χ^{-1}. An interesting observation is that for all plate surface biases the net indirect forces represent a thrust contribution counteracting the increase of direct charged forces with increasing negative surface bias as discussed earlier. A somewhat unexpected result is that the net indirect forces are smaller for the 3-D case resulting in much larger net charged forces compared to the 2-D case. Further analysis of the 3-D

numerical results reveals that indirect force contributions on the ram and wake surfaces are almost equal and acting in opposite directions, canceling each other out (thrust force acting on ram surface and drag force acting on wake surface), whereas the thrust force on the ram surface is much larger than the drag force on the wake surface for the 2-D simulations. This is a direct result of the constrained sheath expansion in the 2-D simulations, which resulted in the formation of a more elongated wake with ions being deflected into smaller angles compared to the 3-D simulations. Further work, both experimental and numerical, is currently ongoing to resolve the observed discrepancies between experimental and numerical data.

CONCLUSION

Charged drag experiments were performed successfully for a negatively charged flat plate immersed in a meso-thermal plasma flow representative of a LEO-like plasma-body interaction. The nano-Newton thrust stand employed in this study was shown to be capable of resolving the incremental changes in the net charged force on the test object with variations of the surface bias applied to the test object. The ion current collected by the charged plate was measured as a proxy for direct momentum exchange between streaming ions and the test object. The combination of force and current measurements has provided experimental evidence for the existence of a counteracting force resulting in a reduction of the direct charged force with increasing surface bias on the test object, which causes the net charged force to level off for surface biases greater than $\approx$ -150 V. From numerical simulations, this effect is related to the electrostatic interaction between the streaming ions and the sheath surrounding the charged test object. The relative sheath thickness compared to the size of the test object was identified as a critical parameter governing the observed behavior. The coupled experimental and numerical investigation presented here is a significant step towards a benchmark-quality ground-based experimental capability for ionospheric aerodynamics research. Such capability in conjunction with our numerical modeling capability represents a powerful research tool to address the gaps in our understanding of the physical processes underpinning plasma-body interactions in the ionosphere in LEO. Further efforts, already on-going, will extend the experimental and numerical work presented in this paper to resolve the discrepancies observed between experimental and numerical data and and further explore the physics of ionospheric aerodynamics.

ACKNOWLEDGMENTS

This research was undertaken with the assistance of resources from the National Computational Infrastructure, which is supported by the Australian Government. This material is based upon work supported by the Air Force Office of Scientific Research award FA2386-17-1-4105.

REFERENCES

[1] National Research Council (NRC), *Continuing Kepler's Quest: Assessing Air Force Space Command's Astrodynamic Standards* (National Academic Press, 2012).
[2] D. E. Hastings, Journal of Geophysical Research **100** (1995).
[3] D. E. Hastings and H. Garratt, *Spacecraft Environment Interactions* (Cambridge University Press, 2004).
[4] C. J. Capon, M. Brown and R. R. Boyce, "Charged aerodynamics of a low earth orbit cylinder," in *30th International Symposium on Rarefied Gas Dynamics*, AIP Conference Proceedings 1786 (2016).
[5] C. J. Capon, M. Brown and R. R. Boyce, Advances in Space Research **62**, 1090–1101 (2018).
[6] C. J. Capon, M. Brown and R. R. Boyce, Physics of Plasmas **24** (2017).
[7] C. M. Cox and F. G. Lemoine, AAS/AIAA Astrodynamics Specialist Conference, AIAA–2008–6442 (2008).
[8] K. Moe and M. M. Moe, Journal of Spacecraft and Rockets **35, No. 3**, 266–272 (1998).
[9] K. Moe and M. M. Moe, Journal of Spacecraft and Rockets **41, No. 5**, 849–853 (2004).
[10] C. L. Brundin, AIAA Journal **1**, 2529–2538 (1963).
[11] G. McHarg, P. Neal, N. Taormina, A. Strom and R. Balthazor, Space Weather **13**, 827–830 (2015).
[12] D. Knechtel and W. C. Pitts, AIAA Aerospace Sciences Meeting **2**, 1148–1151 (1965).
[13] C. J. Capon, "Ionospheric aerodynamics in low earth orbit," Ph.D. thesis, University of New South Wales Canberra 2017.
[14] C. A. Maldonado, S. Rodrigues and A. D. Ketsdever, IEEE Aerospace Conference, 1–11 (2015).

[15] C. A. Maldonado et al., 5th AIAA Atmospheric and Space Environments Conference, AIAA–2013–2681 (2013).
[16] C. A. Maldonado et al., 51st AIAA Aerospace Sciences Meeting, DOI: 10.2514/6.2013–808 (2013).
[17] N. P. Seldon and A. D. Ketsdever, Review of Scientific Instruments **74, No. 12**, 5249–5254 (2003).
[18] C. A. Maldonado and A. D. Ketsdever, 53rd AIAA Aerospace Sciences Meeting, DOI: 10.2514/6.2015–1392 (2015).
[19] C. J. Capon, M. Brown, C. White, T. J. Scanlon and R. R. Boyce, Computers and Fluids **149**, 160–171 (2017).

Appendix C

Experimental Characterization of UNSW Low Earth Orbit Plasma Source (LEOPS)

Introduction

UNSW Canberra Space has recently completed the first stage of commissioning a ground-based experimental ionospheric aerodynamics research capability utilizing UNSW Canberra Space's Low Earth Orbit Plasma Source (LEOPS), procured from Plasma Controls LLC., and the Space Simulation facility (S2F) at the Advanced Instrumentation and Technology Center (AITC) at the Australian National University (ANU) in Canberra, Australia. The LEOPS characterization experiments confirmed that the plasma source is capable of generating the high speed, low density plasma flow required for a faithful simulation of the plasma/body interaction encountered by Low Earth Orbit (LEO) orbiting objects. A range of different plasma diagnostic probes were employed to measure relevant plasma properties, and an in-house designed and built 2-axis remote controllable platform was used to obtain spatially resolved measurements to determine the uniformity of the plasma properties downstream of the plasma source. The results are presented in the following sections.

Work is currently ongoing to commission a nano-Newton force balance similar to the one used for the charged force measurements presented in the publication included in Appendix B.

Experimental Apparatus

The S2F facility utilized for the experimental work presented here is a 3 m diameter and ≈ 4 m long cylindrical stainless steel vacuum chamber, which is capable of attaining a base pressure of $< 3 \times 10^{-7}$ Torr using two 400 mm cryopumps. The cryopumps can be gated off from the vacuum chamber to allow for fast turnaround times. The S2F is equipped with multiple ports to allow for optical access and connection of data and power feedthroughs. A 1.6 m×1.6 m removable platen is available for installation of test setups. The facility setup is described in detail in Ref. [1].

The ability to accurately reproduce Low Earth Orbit (LEO) plasma/body interactions in a ground-based test facility requires the generation of a plasma flow, representative of LEO plasma characteristics, past a stationary test object inside a vacuum chamber, forming a plasma/ionospheric wind tunnel. Representative LEO plasma flow conditions were simulated using the LEOPS originally developed at the Center for Electric Propulsion and Plasma Engineering (CEPPE) located at Colorado State University, Colorado, U.S.A. The design and operation of the source are described in detail in Refs. [2, 3]. Argon gas was used for all tests presented here. The LEOPS was designed to reproduce the meso-thermal plasma flow environment encountered by LEO orbiting objects, where the thermal ion motion in the ambient ionospheric plasma is subsonic with respect to the orbiting body whereas the thermal electrons travel supersonically with respect to the orbiting body. Consequently, ions impact orbiting bodies in the ram direction at orbital velocity (≈ 7.6 km/s) while the electron/body interaction has no preferential direction and is governed by the thermal flux of electrons towards the body. The LEOPS employs a transverse magnetic filter to increase ionization within the source and to prevent high energy electrons from escaping the plasma source to produce a low density meso-thermal plasma flow. The magnetic filter enables operation of the plasma source at low gas flow rates (4 sccm to 10 sccm), which helps to maintain the background pressure inside the vacuum chamber at a sufficiently low level to minimize the likelihood of charge-exchange (CEX) collisions. It is desirable to maintain the vacuum chamber pressure at $\leq 2 \times 10^{-5}$ Torr during plasma source operation. Resonant CEX within the plasma flow exiting the plasma source occurs when the ion/neutral mean free path for Ar^+/Ar collisions is small, which is a function of the vacuum chamber background pressure. CEX collisions cause the streaming Ar^+ ions to lose their energy to adjacent neutral Ar atoms resulting in a bi-modal ion energy distribution function (IEDF). In the extreme case, i.e. at a sufficiently high vacuum chamber pressure, the bulk of the streaming ion energy is lost to neutrals and only thermal, non-streaming ions remain - a scenario to be avoided for a faithful experimental simulation of the LEO plasma flow environment. Figure 1 shows the background pressure inside the S2F recorded for varying flow rates of Argon inside the chamber. Based on these results an Argon gas flow rate of 4 sccm was chosen for all tests to reduce the likelihood of CEX collisions. The chamber pressure readings ranged between 1.5×10^{-5} Torr and 2.1×10^{-5} Torr for the two ion gauges installed on the S2F for all tests.

The LEOPS was mounted onto the internal platen of the S2F via three Aluminium brackets and was positioned approximately in the center of the S2F with the centerline of the LEOPS 415 mm above the platen. The plasma

diagnostic suite comprised a Langmuir probe (LP), Retarding Potential Analyzer (RPA) and Mach Probe (MP). The LP and RPA were mounted on a 2-axis remote controllable positioning system downstream of the LEOPS, while the MP was mounted directly to the internal platen 550 mm downstream of the LEOPS exit plane and 150 mm off the centerline with reference to the center of the MP. A brief description of the plasma diagnostics is provided in the following section. Figure 2 shows the experimental setup inside the S2F.

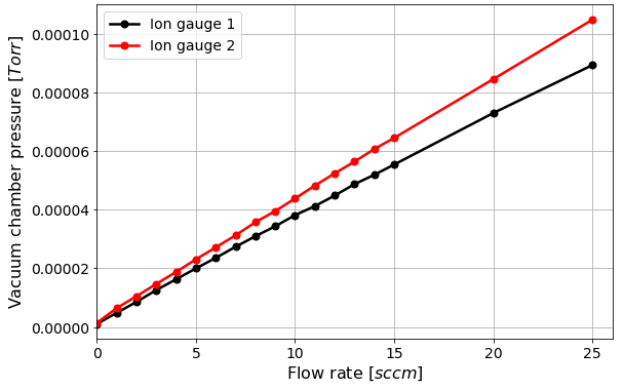

FIGURE 1. Vacuum chamber pressure vs. Argon flow rate characteristic for the S2F facility.

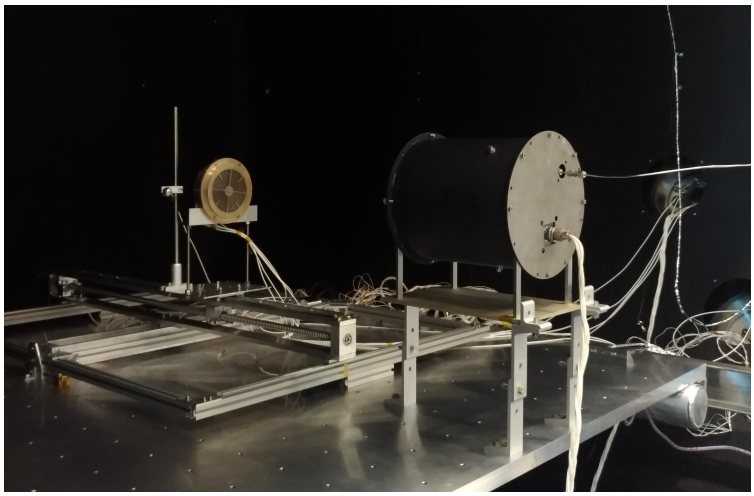

FIGURE 2. LEOPS and plasma diagnostic setup inside the S2F.

Plasma Diagnostics

A spherical LP to measure the plasma density and electron temperature, and a RPA to determine the ion streaming energy and ion temperature have been employed to characterize the plasma flow properties. A Mach Probe was used to verify the existence of a plasma flow. The LP and MP were designed and build in-house while the RPA was procured from Plasma Controls LLC.

A 20 mm diameter spherical Stainless Steel LP, shown in Fig. 3, was used in the tests to obtain plasma density and electron temperature measurements. The large diameter of the probe was chosen in order to be able to employ the thin sheath approximation for the analysis of the LP measurement data. The thin sheath approximation assumes that the sheath thickness is much smaller than the radius, R_{probe}, of the LP. The relevant plasma scale length is the Debye length defined as [4],

FIGURE 3. Langmuir Probe used for LEOPS characterization tests in the S2F.

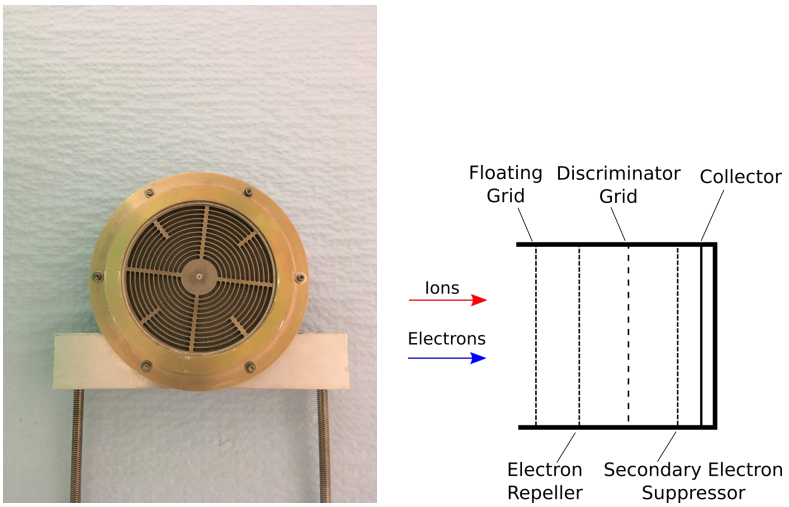

(a) Plasma Controls LLC. RPA. (b) Schematic of internal RPA setup.

FIGURE 4. Retarding Potential Analyzer used for LEOPS characterization tests in the S2F.

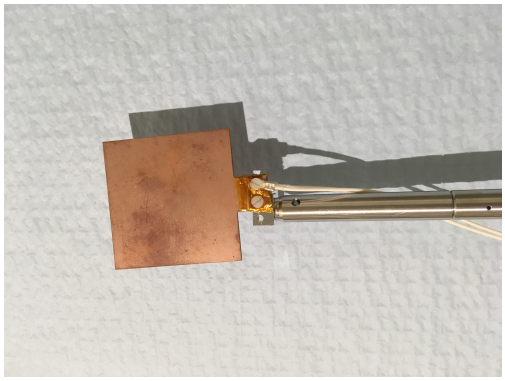

FIGURE 5. Mach Probe used for LEOPS characterization tests in the S2F.

$$\lambda_D = \left(\frac{\epsilon_0 \, k_B \, T_e}{q_e^2 \, n_e} \right)^{1/2}, \tag{1}$$

where ϵ_0 is the vacuum permittivity, k_B is the Boltzmann constant, T_e is the electron temperature, q_e is the elementary electron charge and n_e is the plasma density. Taking into account the plasma quasi-neutrality requirement, the plasma electron and ion densities are considered to be equal, i.e. $n_e = n_i$. For the experiments presented here $\lambda_D \leq 1 \times 10^{-3}$ m and $R_{probe}/\lambda_D \geq 10$ justifying the use of the thin-sheath approximation.

LP voltage sweep and current collection was controlled via a Keithley 6487 voltage source and picoammeter. The voltage sweep range for all LP measurements was -8 V to +10 V. The recorded LP current-voltage (I-V) characteristics exhibit three distinct regions:

1. An electron saturation region for large positive probe voltages above the plasma potential[1]. For spherical probes electron saturation is not fully attained due to the expansion of the sheath around the probe, which increases the effective electron collection volume with increasing probe voltage. In this case, the plasma potential, which separates the electron saturation from the electron retardation region is found from the location of the maximum in the first derivative of the LP I-V characteristic;
2. An electron retardation region, which is dominated by an exponential decay of the electron current to the probe for probe voltages below the plasma potential. The electron temperature can be found from the slope of the I-V characteristic in this region plotted on a semi-log scale;
3. An ion saturation region at large negative probe voltages governed primarily by ion collection below the floating potential[2].

The ion saturation current, used to calculate the ion density, is given by,

$$I_{sat.,i} = exp\,(-0.5)\; q_e \, n_i \, A_{probe} \left(\frac{k_B \, T_e}{m_i} \right)^{1/2} \tag{2}$$

where q_e, is the elementary electron charge, n_i is the ion density, A_{probe} is the current collecting surface area of the probe, k_B is the Boltzmann constant, T_e is the electron temperature and m_i is the ion mass in kg. Equation 2 relies upon the assumption that $T_i \ll T_e$, which is satisfied for the tests presented here (see next section). The equation can then be rearranged to solve for the ion density, n_i. For a spherical LP the I-V characteristic generally has a slight slope to it in the ion saturation region, which is due to the expansion of the sheath with increasing negative probe voltage [5, 6]. Following the approach by Chen [5] the ion saturation current is found by extrapolating the linear part of the ion saturation characteristic back to the floating potential, i.e. the potential where the net current draw of the probe is zero. The reader is referred to Refs. [4, 6] for a detailed description of LP analysis.

A large aperture RPA, procured from Plasma Controls LLC., was used to measure the ion energy distribution of the streaming plasma produced by the LEOPS. The RPA is shown in Fig. 4 (a) and a schematic of the internal electrostatic grid setup is given in Fig. 4 (b). The probe consists of four internal electrostatic grids arranged normal to the oncoming plasma flow. All grids are electrically isolated from the outer casing, which is held at ground/chamber potential. The first grid remains floating to reduce any interference between the other biased grids and the external plasma environment. The second grid was biased at -45 V to repel incoming electrons. The third grid was swept from -6 V to +15 V acting as a high pass filter for the incoming ion stream, which only allows ions with an energy-to-charge ratio greater than the bias on the discriminator grid to pass through and be recorded as collected current by the probe. The fourth grid was biased at -45 V to suppress secondary electrons produced through ion impact on the collector plate. The collector was also biased negatively at -40 V to further reduce secondary electron emission.

The first derivative of the RPA I-V characteristic is proportional to the ion energy distribution function (IEDF) [7],

$$f(E_i) \propto \frac{d\, I_{collector}}{d\Phi_{discriminator}} = -\frac{q_e^2 \, n_i \, A_{collector}}{m_i} \, f(E_i) \tag{3}$$

[1]The plasma potential is the potential that the ambient plasma attains with respect to the vacuum chamber ground reference potential. No sheath develops around objects biased at plasma potential resulting in the current of the probe being governed by the thermal electron flux for positive plasma potentials.

[2]The floating potential is the potential for which the electron and ion current collected by the LP are equal resulting in zero net current draw by the probe.

where E_i is the energy of the ions, $A_{collector}$ is the surface area of the collector plate and all other variables are as defined previously. The distribution function for the streaming ions normal to the RPA can be assumed to take the form of a drifted Maxwellian expressed in terms of energy instead of velocity [7],

$$f(E) = \left(\frac{1}{4\,\pi\,k_B\,T_i}\right)^{1/2} \left(\frac{1}{E}\right)^{1/2} \times exp\left(-\frac{E\ -\ 2\ \sqrt{E\,E_d}\ +\ E_d}{k_B\,T_i}\right), \tag{4}$$

where E_d is the streaming ion energy, and $E = \Phi \cdot q_e$ is related to the RPA discriminator bias. Equation 4 can be fit to the experimental RPA I-V characteristics to obtain estimates for the streaming ion energy and the ion temperature. The ion velocity, u_i, can then be calculated as

$$u_i = \sqrt{\frac{2\,E_d}{m_i}}. \tag{5}$$

The Mach probe used for the tests, shown in Fig. 5, was a 50 mm square double-sided copper circuit board with a layer of non-conductive FR4 in between the two layers of copper. This allowed the current collected on the front and rear surfaces to be measured separately. Each surface was electrically isolated from the probe support structure and connected to a picoammeter outside the S2F via a vacuum electrical feedthrough. The MP surfaces were allowed to float relative to the facility electrical ground. Using a MP, it is possible to determine the streaming ion velocity perpendicular to the MP ram side [8]. However, an accurate measurement of the ion velocity requires precise knowledge and modeling of the sheath structure around the probe and the particle trajectories within the sheath. For the present experiments ion streaming velocities were determined from RPA measurements and MP measurements were conducted simply to verify the presence of a plasma flow.

LEOPS Characterization Results and Discussion

Stable LEOPS operation was achieved for a constant discharge current of 5 A and discharge voltage of approx. 42.5 V. An Argon flow rate of 4 sccm was chosen to reduce the likelihood of CEX collisions as described in the previous section. Varying the discharge current below and above 5 A resulted in either unstable plasma source operation with large fluctuations in discharge voltage, or non-repeatable, largely varying plasma property measurements. The source of these instabilities is not currently known and being investigated at the moment. Therefore, the LEOPS characterization results are presented only for the single operating condition stated above. The resulting plasma flow condition closely matches the test condition for the charged force measurements discussed in the publication included in Appendix B.

MP measurements were conducted to verify the existence of a flowing plasma from the LEOPS. A distorted sheath structure develops around objects immersed in a flowing plasma. On the ram facing side, the sheath is compressed due to the high speed impact of ions. On the wake side, the sheath is elongated due to an ion void or negative space-charge region that forms immediately behind the object. The ion void is a result of the faster moving electrons being able to populate the region behind the object more easily than the slower moving ions. This is illustrated in Fig. 6, which shows collected current measurements on the front and rear surfaces of the MP over a period of 5 seconds. The negative current on the front surface indicates ion collection whereas the small positive current on the rear surface is entirely due to electron collection and confirms the presence of an ion void region established behind the MP characteristic for an object immersed in a flowing plasma as described above.

A further verification of plasma flow can be attained by taking measurements with the RPA facing the oncoming plasma flow directly and with the RPA rotated 90° relative to the streaming plasma. In the presence of an accelerated ion population, these two measurements will vary by the location of the peak in the IEDF. At an angle of 90° the location of the peak in the IEDF will provide an estimate of the plasma potential as a result of thermalized ions from CEX collisions being accelerated by the local plasma potential. The absolute magnitude of the collected current will be significantly reduced compared to the current collected with the RPA facing the plasma flow directly as there is no preferential direction for the acceleration imparted by the plasma potential and due to the low levels of CEX occurring at the low vacuum chamber pressure. Figure 7 compares the IEDF's from two representative RPA measurements clearly showing the presence of an accelerated ion population in the IEDF obtained for the RPA facing the plasma flow directly (red curve). The peak location in the IEDF obtained from the measurement with the RPA at 90° (purple curve) is indicative of the plasma potential as described above, and the distribution rapidly drops off for

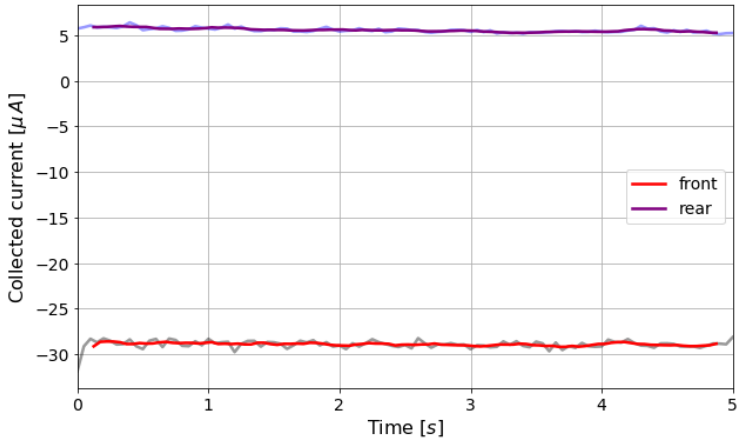

FIGURE 6. Mach Probe collected current measurement.

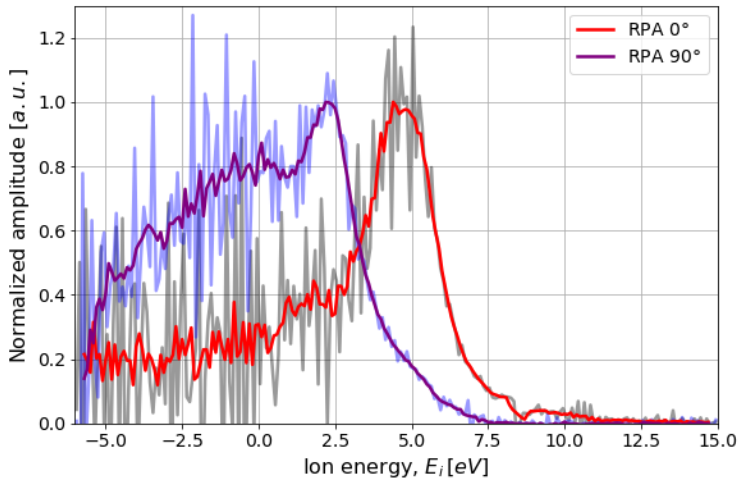

FIGURE 7. Ion energy distribution functions obtained from measurements for RPA orientation of 0° and 90° to the plasma flow.

higher ion energies. These results thus corroborate the conclusion drawn from the MP results. Note that both IEDF's are normalized with their respective peak values to enable a meaningful comparison.

The drifted Maxwellian curve fitting approach described in the previous section was applied to the IEDF's obtained from the RPA measurements to determine the ion streaming energy and associated velocity, and the ion temperature. Figure 8 shows a sample IEDF and the drifted Maxwellian least-squares curve fit based on Eqns. 3 and 4, which shows that the measured energy distribution of the accelerated ion population is reasonably well approximated by a drifted Maxwellian. Figures. 9 (a) and (b) show the axial variation of the streaming ion energy and ion temperature, expressed in [eV][3], downstream of the LEOPS exit plane. The error bars represent 95% confidence intervals with respect to the average values obtained from ten separate measurements at each measurement location. The ion streaming energy and temperature vary only slightly with downstream distance and remain fairly constant, ranging between 4.8 eV and 4.9 eV, from approximately 0.6 m downstream of the LEOPS exit plane. This is an important result. As will be seen below, test objects can thus be placed at different downstream locations to conduct tests at different plasma densities while maintaining the relative kinetic energy of the plasma flow.

[3]Ion and electron temperatures are often expressed in unit of [eV] instead of [K]. These are equivalent and the conversion is achieved via T [eV] = T [K] $\cdot(k_B/q_e)$.

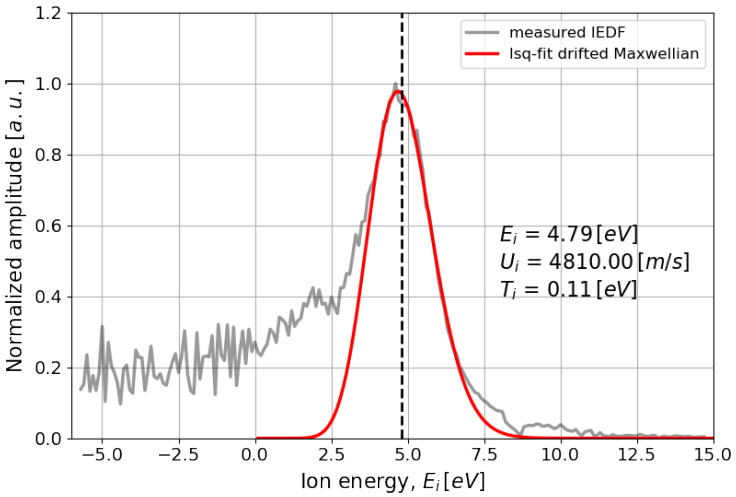

FIGURE 8. Drifted Maxwellian curve fit to measured ion energy distribution function, based on Eqn. 4.

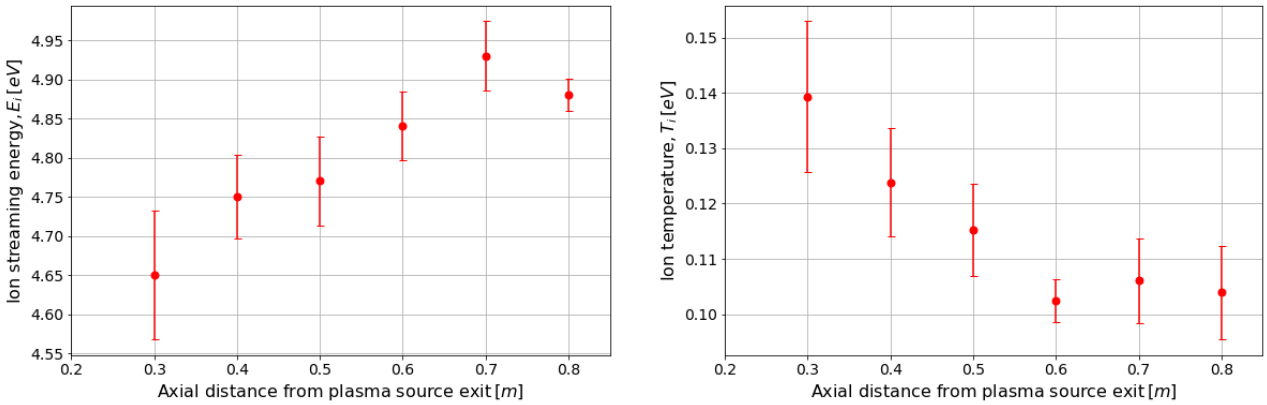

(a) (b) .

FIGURE 9. Axial variation of (a) streaming ion energy and (b) ion temperature downstream of LEOPS exit plane.

At the tested operating conditions, the LEOPS produces a flowing plasma with an accelerated ion population at ≈ 4.9 eV, which matches the relative kinetic energy of ambient ionospheric ions with respect to LEO orbiting objects, assuming an average circular orbital velocity of 7.6 km/s in LEO. The ion temperatures derived from the drifted Maxwellian curve fit shown in Fig. 9 (b) range between 0.1 eV and 0.14 eV. These values are also representative of ionospheric ion temperatures for solar maximum conditions [9].

Finally Figs. 10 (a) and (b) show axial and lateral ion density distributions downstream of the LEOPS exit plane, respectively. Axial density measurements were conducted between 0.3 m and 0.8 m downstream of the LEOPS exit plane. The lateral ion density measurements were taken at a distance of 0.55 m downstream of the LEOPS exit plane at 20 mm intervals. The error bars represent 95% confidence intervals with respect to the average values obtained from five separate measurements at each measurement location. Ion densities decrease with downstream distance ranging from $\approx 2.9\times10^{14}$ m^{-3} at 0.3 m downstream of the LEOPS exit plane to $\approx 4\times10^{13}$ m^{-3} at 0.8 m downstream of the LEOPS exit plane. The lateral ion density measurements indicate that the plasma flow is well collimated and ion densities are approximately uniform over a distance of 120 mm off the centerline.

Figures 11 (a) and (b) show axial and lateral variations of the electron temperature at the same measurement

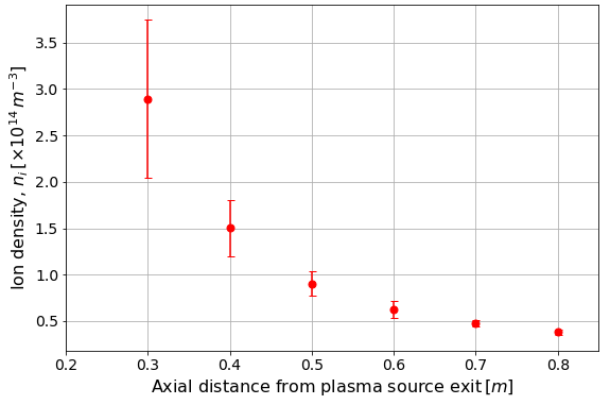

(a) Axial variation.

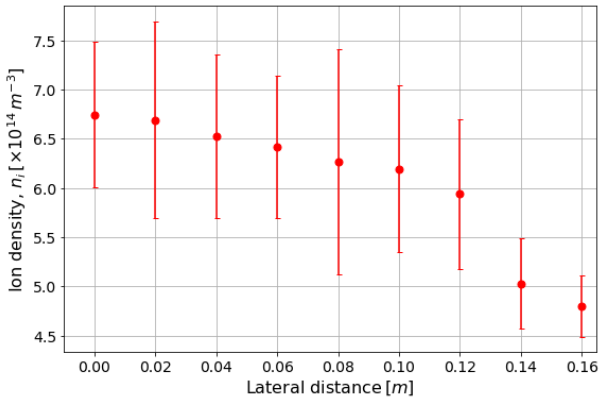

(b) Lateral variation 0.55 m downstream of LEOPS exit plane.

FIGURE 10. Ion densities obtained from LP measurements downstream of LEOPS exit plane.

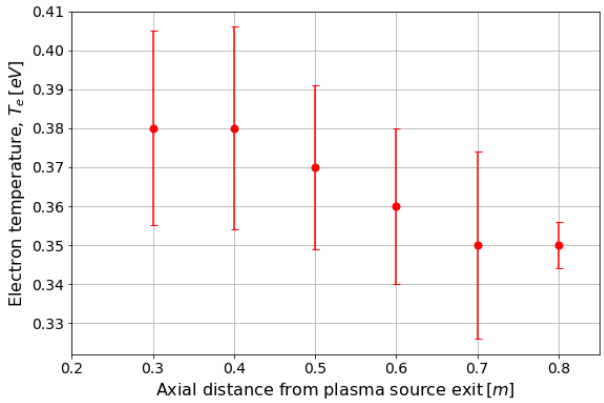

(a) Axial variation.

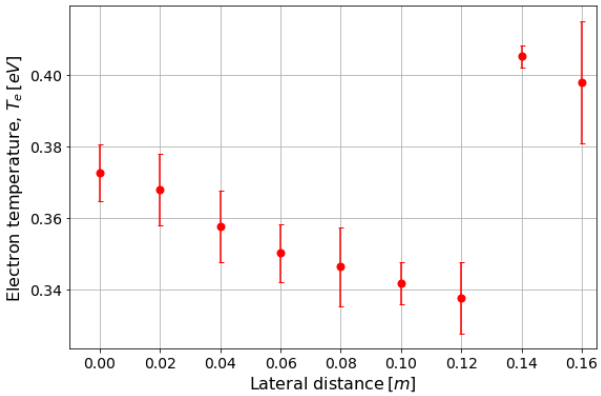

(b) Lateral variation 0.55 m downstream of LEOPS exit plane.

FIGURE 11. Electron temperatures obtained from LP measurements downstream of LEOPS exit plane.

intervals as for the ion density measurements. The error bars represent 95% confidence intervals with respect to the average values obtained from five separate measurements at each measurement location. Electron temperatures can be seen to decrease slightly with increasing distance from the plasma source exit, ranging from ≈ 0.38 eV at 0.3 m to ≈ 0.35 eV at 0.8 m downstream of the LEOPS exit plane. A similar variation can be observed in the lateral direction until approximately 120 mm off the centerline beyond which point electron temperatures increase to around 0.4 eV. Further, the LP I-V characteristics for lateral distances greater than 120 mm showed a distinct bi-Maxwellian electron distribution, with two straight line sections in the electron retardation region when plotted on a semi-log scale. The LP measurements support the findings from the RPA measurements that the plasma flow properties are reasonably uniform over a distance of approximately 120 mm off the centerline.

The measured ion densities and electron temperatures are slightly larger than typical representative ionospheric values [9]. Note, however, that actual particle densities and temperatures within the ionosphere are subject to significant variations depending on the time of day, latitude, longitude, altitude, solar activity and many other factors. An important part of any ground-based experimental research is an understanding of the relevant scaling parameters for the physical problem under consideration to guarantee representative test conditions. Through dimensional analysis applied to the governing equations for LEO plasma/body interactions - the collision-less Boltzmann (Vlasov) equation and Poisson's equation with a Boltzmann electron fluid - Capon et al. [10] derived and applied a generalized

set of scaling laws that describe meso-thermal plasma/body interactions to map out key physical phenomena that influence ionospheric aerodynamic forces. Two key dimensionless parameters were shown to govern the ionospheric aerodynamic behavior, given in Eqn. 6 and 7,

$$\alpha = -\frac{q_e \Phi_B}{m_i u_i^2} \tag{6}$$

$$\chi = \frac{r_B}{\lambda_\Phi},\ \lambda_\Phi = \left(-\frac{\epsilon_0 \Phi_B}{q_e \Sigma_i n_i} \right)^{1/2} \tag{7}$$

where Φ_B is the object surface potential, q_e is the elementary charge, ϵ_0 is the vacuum permittivity, r_B is a characteristic object dimension (e.g. the radius of a spherical object), and m_i, u_i and n_i are the ion mass, streaming velocity and density, respectively. Therefore, while the experimental test flow does not precisely replicate the actual flow conditions within the ionosphere, it nevertheless contains the relevant physical processes provided care is taken in observing the relevant scaling parameters described above when planning and setting up the tests.

The results presented here demonstrate that the developed experimental capability is suitable for a faithful simulation of the LEO ionosphere plasma environment and presents a significant step towards a benchmark-quality ground-based experimental capability for ionospheric aerodynamics research.

REFERENCES

[1] M. Petkovic and R. Pollara, "Dual-purpose space simulation facility for plasma thruster and satellite testing," in *28th Space Simulation Conference* (2014).

[2] J. D. Williams et al., "Ground-based simulation of low earth orbit plasma conditions: Plasma generation and characterization," in *8th Spacecraft Charging Technology Conference* (2003).

[3] B. Rubin et al., Plasma Sources Science and Technology **18**, doi:10.1088/0963–0252/18/2/025015 (2009).

[4] I. H. Hutchinson, *Principles of Plasma Diagnostics* (Cambridge University Press, 2002).

[5] F. F. Chen, J. D. Evans and D. Arnush, Physics of Plasmas **9**, p. https://doi.org/10.1063/1.1462630 (2002).

[6] R. Merlino, American Journal of Physics **75**, p. https://doi.org/10.1119/1.2772282 (2007).

[7] C. L. Enloe et al., Review of Scientific Instruments **66**, p. https://doi.org/10.1063/1.1145367 (2002).

[8] J. K. McTernan, "Passive plasma contact mechanisms for small-scale spacecraft," Ph.D. thesis, The Pennsylvania State University 2017.

[9] D. E. Hastings, Journal of Geophysical Research **100** (1995).

[10] C. J. Capon, M. Brown and R. R. Boyce, Physics of Plasmas **24** (2017).